Fibre Sensing

Tay Wei Yau, Thormund
A0136214R
Department of Physics, Faculty of Science
National University of Singapore

Supervisor:
Professor Christian Kurtsiefer

In partial fulfillment of the requirements for the degree of
Bachelor of Science (Hons)
2022

Acknowledgements

Over the course of this project, I've suffered a cornea abrasion resulting in temporary blindness, a hard disk failure of my laptop of many years from processing all the data collected from the experiment, and a symptomatic case of COVID-19 for 8 days, longer than the recommended policies' expectations. If not for the support of everyone, the extent of the project would not have been as far as it presently is, and for that, I am grateful to everyone that has supported me along this journey.

In no particular order, I would like to express my greatest gratitude to the following people.

Firstly, I would like to thank Prof. Christian Kurtsiefer for giving me the opportunity to work on such an exciting project that was within my skillset.

Next, I would like to thank my mentor Dr. Shi YiCheng for the invaluable support, both in the project and my various circumstances throughout the year.

Lastly, I would like to thank my friends, particularly Jun Yan and Ariana, for the support, the endless amount of ideas for this project that I could bounce off, and the guidance of the several important technical skills that helped me bounce off from my dead computer within 4 days despite these period of severe computer chip shortages.

Abstract

A fiber-based Michelson interferometer is capable of measuring sub-micrometer changes in its optical path difference, and can be utilized for sensing mechanical perturbations in the environment. Such an interferometer can be modified to a heterodyned phasemeter by placing an acousto-optical frequency shifter in one of the interfering arms, which allows unambiguous measurements of the directional displacements in the optical path difference.

This thesis describes the development and optimizations of such a fiber-based heterodyne phasemeter operating at telecommunication wavelength (1550 nm). In this phasemeter, the optical path differences between the two interfering arms are encoded into the phase of a beatnote between two different optical frequencies. The phase information is extracted through a digital I/Q demodulation scheme, which involves sampling the beat signal at a specific frequency. This allows for an accurate reading of the length difference between the two arms of the interferometer.

List of Figures

Contents

Chapter 1

Introduction

1.1 Recent Developments in Underwater Seismology

71% of the Earth's surface is covered by water, posing major logistical challenges for geophysical research in the Earth Science community. As such, majority of seismic stations are located on land, with limited numbers of temporary ocean-bottom seismometers[1, 2], and permanently tethered observatories[3]. However, these systems are very costly and often unfeasible on large scales.[4]

With the rise of the internet, most oceans are crossed by an extensive infrastructure of telecommunication fibres.[5] In 2012, an international Joint Task Force was established to design "SMART" (Scientific Monitoring and Reliable Telecommunications) cables with environmental sensors embedded in repeaters every $\sim$50 km.[6, 7] Since, there has been efforts to turn these optical fibres into seismo-acoustic sensors. A breakthrough is shown in Marra et al. [4], coincidental detection of earthquakes via analyzing the phase stability of the metrology-grade lasers has shown this method to be successful with optical fibres with lengths on the order of 1000 km. However, the author acknowledges that in the case of a single optical fibre, there is ambiguity in determining the location of seismic events, which can only be resolved with the use of a second optical fibre located elsewhere.

An alternative method known as Distributed Acoustic Sensing (DAS)[8–11], analyses backscattered laser light with phase-based optical time domain-reflectometry[12] to resolve seismic activity detected to within the fibre[8, 9]. This method has been successful at mapping out previously unmapped fault zones with a single optical fibre.[8] However, DAS as a method is only feasible with much shorter optical cables, on the order of 20 km due to attenuation.[12–14]

With these considerations, this thesis proposes the development and improvement of a fibre-based interferometric system that can detect mechanical perturbations.

1.2 Thesis Outline

The thesis aims to describe the development and optimisations of a digital fibre-based interferometric system, called the *heterodyne phasemeter*[15].

In Chapter 2, the well-known Michelson interferometer[15] is first introduced, before highlighting on its limitations. This gives rise to the modification of the interferometer to produce a heterodyned phasemeter in Chapter 3. However, the signal from heterodyned phasemeter is modulated unlike the Michelson interferometer, and a demodulation scheme—I/Q demodulation is introduced in theory.

Chapter 4 discusses some experimental results that follows from using I/Q demodulation, and complications that arises in such an experimental setup. Chapter 5 then experiments with a different demodulation scheme, and describes some of the results.

Chapter 2

Michelson Interferometer Setup

2.1 Fibre-based Michelson Interferometer

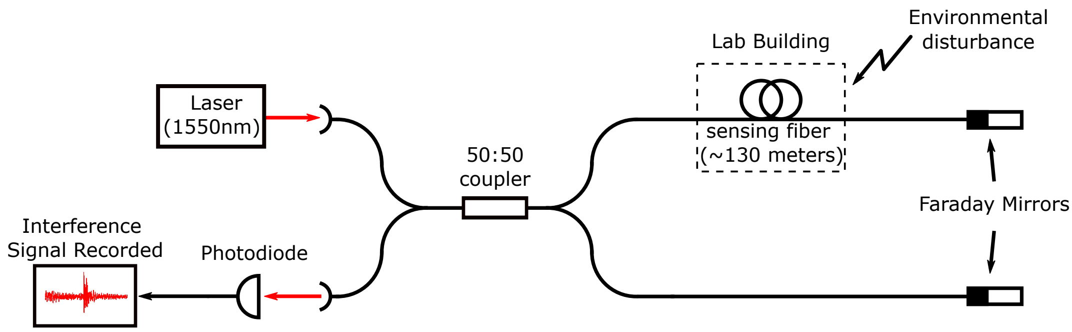

Figure 2.1: Fibre-based Michelson Interferometer

Figure 2.1 is a schematic diagram of a fibre-based Michelson interferometer. We begin with the use of a coherent light source—a laser. Denote the electric field into the interferometer by E_{in}, with power P_{in}, with a wavelength $\lambda_0 = 1550$ nm. The optical index of the optical fibre core has value $n = 1.52$, and the wavenumber of the light within the circuit is $k = nk_0 = n\frac{2\pi}{\lambda_0}$. To avoid back reflection into the laser, the light is passed through an optical isolator.

The laser light is then passed through a 50:50 coupler. Here, the coupler acts as a beam splitter, and the laser light passes through both fibre-arms of the interferometer, with lengths L_x and $L_y = L_x + \Delta L$.

Due to birefringence [16, 17], the state of polarization is altered as it travels through an optical fibre. If the light was simply reflected off a regular mirror, the light that exits each arm of the Michelson interferometer could be in sufficiently distinct polarization states such that the interference may not produce a distinct interference pattern. This can be compensated with the use of a Faraday mirror at the end of each arm of the Michelson interferometer. In a Faraday Mirror, the electric field gains a $\pi/4$ rad rotation in polarization state as it passes between the Bismuth Iron Garnet (BIG) Faraday Rotating element, before being reflected off the mirror, and another $\pi/4$ rad as it passes through the BIG magnets once more. As such, light that reflects off a Faraday mirror has a effective $\pi/2$ rad rotation in its state of polarization with respect to the input state. Any perturbation that is picked up by the laser light from the birefringence in the optical fibre will therefore be reversed during the return trip. As such, the laser light that is emitted from both arms of the interferometer has polarization state that is orthogonal to the the light that had entered each arm. This allows for a strong interference between the laser light from both arms of the interferometer.

Here, the light would have traveled down $2L_x$ in one arm, and $2L_x + 2\Delta L_x$ in the other arm. They superpose together at the 50:50 coupler, and exits the interferometer to be detected by the photodiode. The electric field at the output of the interferometer is given by

$$E_{\text{out}} = \frac{1}{2}E_{\text{in}}\left(e^{i2kL_x} + e^{i2kL_y}\right).$$

At this point, it is convenient to define the optical phase difference

$$\phi_d = 2k\Delta L, \tag{2.1}$$

which allows us to rewrite the outgoing electric field and measurable power as[18]

$$E_{\text{out}} = \frac{1}{2}E_{\text{in}}e^{i2kL_x}\left(1 + e^{i\phi_d}\right), \tag{2.2}$$

$$P_{\text{out}} = \frac{P_{\text{in}}}{4}\left[4\cos^2\left(\frac{\phi_d}{2}\right)\right] = \frac{P_{\text{in}}}{2}\left[1 + \cos\phi_d\right]. \tag{2.3}$$

The output optical power from the interferometer is therefore proportional to the laser power into the interferometer, and is a sinusoidal of the optical phase difference ϕ_d.

Ambiguous Relative Length Changes A direct observation of Equation (2.3) shows that the power measured by the photodiode is periodic with respect to the optical phase difference ϕ_d, and consequentially, periodic with respect to the relative length difference between the 2 arms of the interferometer. A graphical interpretation is as given in Figure 2.2.

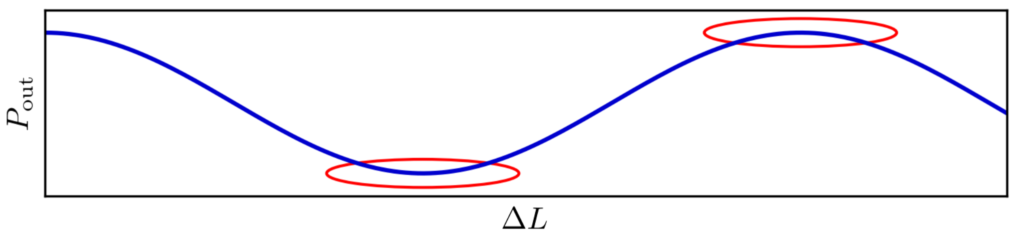

Figure 2.2: Visual representation of power against optical phase difference

If the power fluctuation due to the length changes is small, there is no issue with such an experimental setup to detect relative length changes, provided the intial outgoing power is far from the extrema points as circled within Figure 2.2.

However, at the extrema of the cosine function, such as those circled within Figure 2.2, any change (both increase and decrease) in ΔL, produces the same change in P_{out}. As such, there an is *ambiguity* in the increase or decrease in ΔL for a given change in P_{out} from its extrema. With extended measurement, there is greater ambiguity in the relative length changes ΔL of the fibre if the output optical power from the interferometer is near an extrema point.

Chapter 3

Heterodyned Phasemeter and Demodulation

This section will first describe my experimental setup to modulate the optical phase difference into a carrier signal, followed by 2 different methods to demodulate the phase information from the carrier signal.

3.1 Heterodyne Phasemeter Setup

While a conventional Fibre-based Michelson interferometer is able to measure sub-micrometer changes in optical fibre length, it is ambiguous at measuring the displacement near the extrema in output power. The heterodyned phasemeter is able to solve this issue. An unambiguous optical phase ϕ_d (equivalently, displacement ΔL) is made possible by interfering electric fields with two different frequencies within the interferometer. A different optical frequency from the input laser can be provided through a frequency shifter, based on an acousto-optic modulator (AOM). Figure 3.1 shows a schematic of my experimental setup.

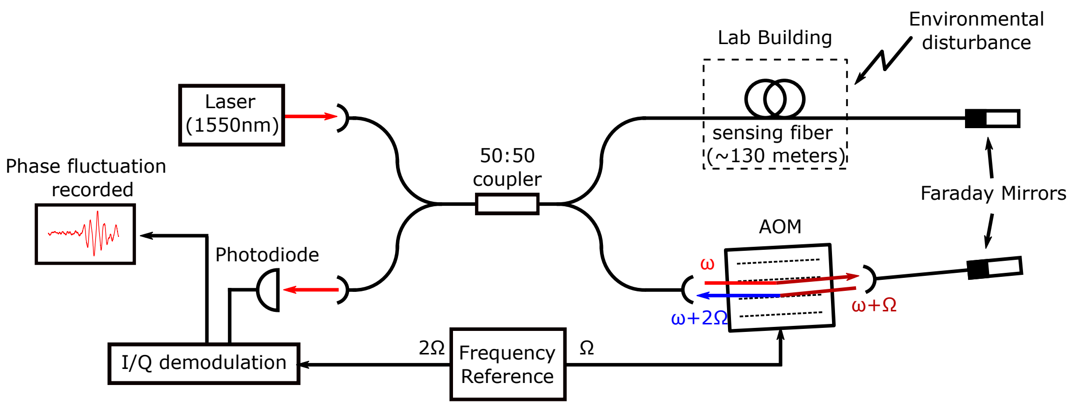

Figure 3.1: Heterodyne Phasemeter

In contrast to the fibre-based interferometer, this experimental setup includes the use of an AOM in the control arm of the 'interferometer', giving a phasemeter. This phasemeter is said to be 'heterodyne', as it utilises 2 frequencies to determine the phase of the interference signal.

Similar to the previous chapter, the laser light entering the interferometer is first split into both arms of the interferometer by the 50:50 coupler. Along the control arm, the AOM is connected to a frequency reference, which is set to some frequency f_{AOM}. The light in the control arm, before passing through the AOM, has some angular frequency $\omega = kc$. The first order diffraction through the AOM gains the angular frequency $\Omega = 2\pi f_{\mathrm{AOM}}$ to then have a total angular frequency of $\omega + \Omega$, before traveling further down the optical fibre and reflected off the Faraday mirror. The same process is repeated once more as it passes down the AOM a second time on its way to the 50:50 coupler, giving rise to a total angular frequency of $\omega + 2\Omega$ in the light outgoing from the control arm of the interferometer.

The light from the control arm then interferes with light from the sensing arm at the 50:50 coupler, which creates an optical beat signal.

Expected Signal By considering the linear superposition of the outgoing light from each interferometer arm, the expected electric field as a function of time is given by

$$E_{\mathrm{out}}(t) = \frac{1}{2}E_{\mathrm{in}}\left(e^{i(\omega t - \phi_d/2)} + e^{i(\omega t + 2\Omega t + \phi_d/2)}\right).$$

Utilising the optical phase difference definition in Equation (2.1), the equation is simplified to[18]

$$E_{\mathrm{out}}(t) = \frac{1}{2}E_{\mathrm{in}}e^{i(\omega t - \phi_d/2)}\left(1 + e^{i(2\Omega t + \phi_d)}\right). \tag{3.1}$$

Therefore, the power P_{out} that exits the phasemeter is given by

$$P_{\mathrm{out}}(t) = \frac{P_{\mathrm{in}}}{2}\left[1 + \cos\left(2\Omega t + \phi_d\right)\right]. \tag{3.2}$$

As such, for fixed optical phase difference ϕ_d, the output power from the phasemeter is an optical beat signal with frequency $f = 2\Omega/2\pi$.

Physical Devices Used The laser source used in this project is a Thorlabs SFL1550S laser. This laser is based on an external cavity configuration, with a lasing wavelength of 1550 nm. In the given configuration, the laser generates a power output approximately 5 mW. The power that exits the interferometer is approximately 2 mW. The laser linewidth was measured utilising the self-heterodyne method. This method involves optically beating the laser with a delayed portion of itself in an incoherent manner. The provided delay needs to be larger than the estimated coherence time of the laser itself.

In this case, we set the interferometer to an imbalanced configuration, with one arm connected to 1 km long fibre spool, and the other arm to a 6 m fibre patch-cord. The power spectrum of the optical beatnote was measured with a spectrum analyzer, and is shown in Figure 3.2.

When the light interferes with itself incoherently, the measured linewidth of the optical beatnote is twice of the natural linewidth of the laser itself. In Figure 3.2, the spectrum was fitted with a lorentzian profile, and the full width at half maximum (FWHM) was found to be about 490 kHz. As such, we deduce that the laser linewidth is about 245.1(9.2) kHz, which corresponds to a coherence length of about 389 m.

The AOM used in this setup is from Brimrose (AMF-80-20-1550). At different driving frequencies, the first order diffraction efficiency of the AOM is shown in Figure 3.3. In this

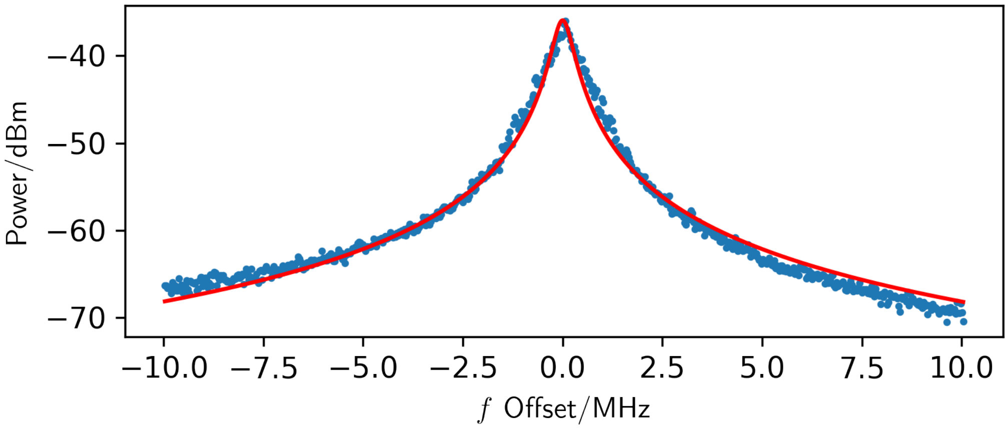

Figure 3.2: The measured power spectrum (with resolution bandwidth of 31 kHz) is fitted to a Lorentzian distribution. The corresponding FWHM of the fit is found to be about 490 kHz. The optical linewidth of the laser is therefore about 245.1(9.2) kHz.

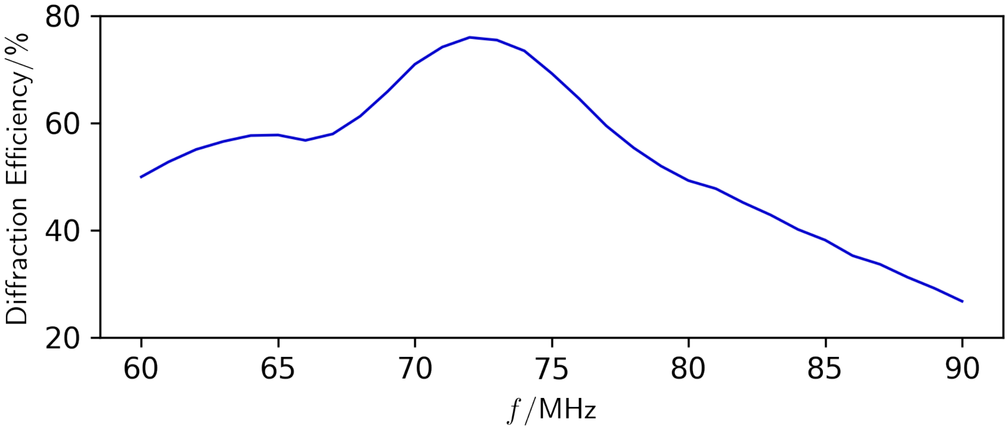

Figure 3.3: The first order diffraction efficiency is measured as the ratio between the first order output power and the input power into the AOM. The AOM is found to be most efficient around 70 MHz.

experiment, the AOM driving frequency f_{AOM} was therefore chosen to be around 70 MHz, unless otherwise stated.

The output optical beatnote is detected with a fast InGaAs (Indium gallium arsenide) photodiode (GAP100FC from GPD optoelectronics).

3.2 I/Q Demodulation by Analogue Circuit

In the previous section, it has been shown that phase information (optical phase difference ϕ_d) has been encoded as the phase of the optical beatnote. In this section, a scheme that demodulates this optical beat signal to obtain the phase information will be described.

This demodulation process is commonly known as I/Q demodulation, and an I/Q demodulator can be constructed using analogue components, such as mixers and low pass filters. An

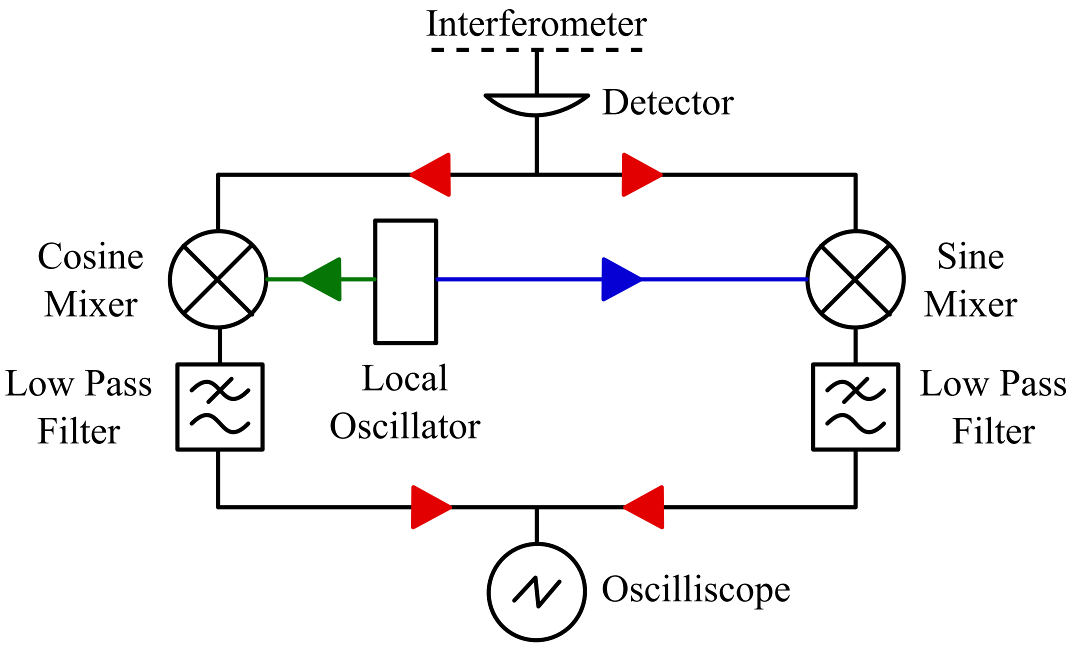

Figure 3.4: Schematic diagram of demodulator circuit.

example of such a demodulator is shown in Figure 3.4. A direct digital synthesizer (DDS) generates a strong sinusoidal signal at twice of the AOM driving frequency ($f = 2f_{\text{AOM}} \approx 140\,\text{MHz}$). This signal, also known as the local oscillator, is split into two via a power splitter. The two split signals are directed into two RF mixers, with one signal being phase delayed by $\pi/2$ rad relative to the other signal. In the meantime, the optical beat signal measured from the photodiode is also split and sent into the two mixers. The mixer performs a multiplication between the two inputs.

For the first mixer (cosine mixer in Figure 3.4), the output signal is given by[18]

$$P_{\text{out}}(t) \cdot \cos 2\Omega t = \frac{P_{\text{in}}}{2}\left[2\cos 2\Omega t + \cos(4\Omega t + \phi_d) + \cos\phi_d\right],$$

where $2\Omega = 2\pi f = 4\pi f_{\text{AOM}}$. In the other mixer (sine mixer in Figure 3.4), the output signal is given by

$$P_{\text{out}}(t) \cdot \sin 2\Omega t = \frac{P_{\text{in}}}{2}\left[2\sin 2\Omega t + \sin(4\Omega t + \phi_d) - \sin\phi_d\right].$$

We can easily observe that the output signal in the previous expressions from both mixers contain not only the sine/cosine value of the optical phase difference ϕ_d, but also the local oscillator frequency 2Ω and its higher harmonic. The high frequency terms $(2\Omega, 4\Omega)$ can be easily removed with an appropriate low pass filter, leaving only the $\cos\phi_d, -\sin\phi_d$ terms. This gives the I, Q components to be

$$I = \frac{P_{\text{in}}}{2}\cos\phi_d, \quad Q = -\frac{P_{\text{in}}}{2}\sin\phi_d, \tag{3.3}$$

and optical phase difference calculated to be

$$\phi_d = \tan^{-1}\left(\frac{-Q}{I}\right). \tag{3.4}$$

From the previous section, note that measuring the phase allows one to determine the length changes within the interferometer.

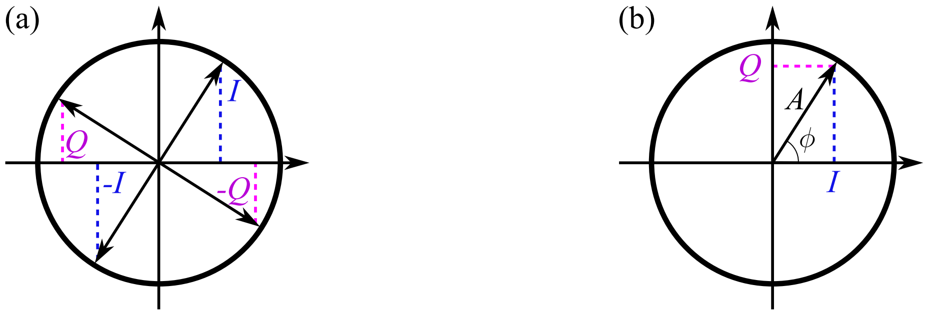

(a) A phasor rotating over time.

(b) The I and Q component of a phasor.

Figure 3.5: A sinusoidal wave can be represented by a rotating vector of amplitude A, with phase ϕ.

With reference to Figure 3.5, a sinusoidal wave can be represented by a rotating vector, with its amplitude being the length of the vector A, and its phase being the argument of the vector ϕ. The I, Q components are merely projections of this vector onto the x, y axes. This representation is commonly known as a phasor diagram.

3.3 Digital I/Q Demodulation

While such a circuit as described in Section 3.2 is capable of demodulating the signal, the setup requires an assembly of passive components and a physical RF source as the local oscillator. While this physical setup can be made compact, there exists a digital alternative which significantly simplifies the demodulation procedure. For this section, a general observation is made on sinusoidal functions, before explaining its implication on our experimental setup, and hence, the choice of sampling scheme.

Mathematical Description We begin with a different interpretation of the I/Q components of a signal. Assume we have an arbitrary sinusoidal signal $y(t)$ with an angular frequency $\omega = 2\pi f$, and an amplitude A. One can express $y(t)$ as

$$y(t) = A\sin(\omega t + \varphi_0) \tag{3.5a}$$

$$= \underbrace{A\cos\varphi_0}_{I}\sin\omega t + \underbrace{A\sin\varphi_0}_{Q}\cos\omega t, \tag{3.5b}$$

$$= I\sin\omega t + Q\sin(\omega t - \pi/2). \tag{3.5c}$$

Here, we see that the quadrature-phase term Q lags the in-phase term I by $\pi/2$.

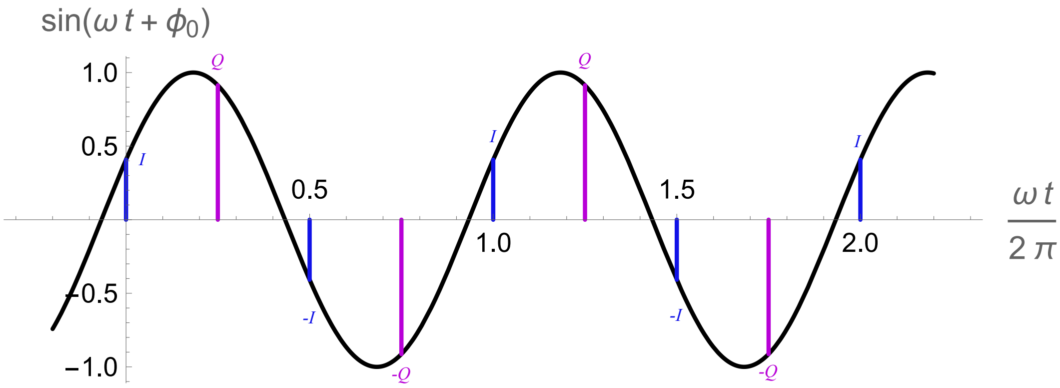

Figure 3.6: Reading of I, Q components directly off a sinusoidal wave.

If one measures this signal $y(t)$ at times t such that ωt is a multiple of $\pi/2$, one can easily extract the I, Q components, as exemplified in Figure 3.6, where[19]

$$\begin{aligned} \omega t_0 &= 0, & y(t_0) &= \quad I; \\ \omega t_1 &= \pi/2, & y(t_1) &= \quad Q; \\ \omega t_2 &= \pi, & y(t_2) &= -I; \\ \omega t_3 &= 3\pi/2, & y(t_3) &= -Q. \end{aligned}$$

There is an implicit assumption that the amplitude A and phase φ of the signal does not change abruptly between consecutive samples.

With some observation of Figure 3.6, (or perhaps the 2π periodicity of $\omega t \to \omega t + 2\pi$ on Equation (3.5)), one would be able to make the justified remark that the Q value as read off $y(t_1)$ where $\omega t_1 = 0.25 \cdot 2\pi$ to be no different from the Q value as read off $y(t_5)$ where $\omega t_5 = 1.25 \cdot 2\pi$. Explicitly, for any sampled value at time t_i, the next value can be sampled at time t_{i+1} with $\omega\,(t_{i+1} - t_i) = (m + 1/4) \cdot 2\pi$, where m is a natural number. As such, the sampling frequency f_s no longer needs to be 4 times the frequency of the sinusoidal, but any frequency f_s that satisfies

$$f_s = \frac{N}{M} f,$$

with rational N/M, such that $N = 4$.[19]

Regardless of the time t_i where ωt_i is some multiple of $\pi/2$ when the sinusoidal was measured, the phase offset φ_0 is always given by

$$\varphi_0 = \tan^{-1}\left(\frac{Q}{I}\right) \tag{3.6}$$

in this convention.

Digital I/Q Demodulation with Lower Sampling Frequencies With reference to the mathematical description, the experimental setup demands that the output optical beat needs to have a stable amplitude, and the change in optical path difference in the interferometer has to happen at a much lower frequency than the AOM and sampling frequency.

In our experimental setup, the shift in optical frequency is $f = 2 f_{\text{AOM}} \approx 140\,\text{MHz}$. This translates to a high sampling frequency $f_s = 4f \approx 560\,\text{MHz}$, by constraint of $\Delta t = t_{i+1} - t_i = \pi/2\omega$ in the initial description. Such a high sampling frequency which will generate an excessive amount of data. As such, we wish to reduce the sampling frequency, which the mathematical description permits by choice of $f_s = \frac{4}{M}f$, where M is an integer one is free to choose.

Sampling Scheme This gives rise to our choice of sampling scheme. With reference to Equation (3.2), we expect the measurement on the power emitted from the interferometer to be a sinusoidal with frequency $f \approx 140\,\text{MHz}$. As prior established, while it is possible to choose a sampling frequency f_s to be $4f \approx 560\,\text{MHz}$, at this high frequency the setup generates a dense data set. We can instead choose a more conservative lower sampling frequency, such as on the order of MHz. In the case of sampling frequency $f_s = 1.0\,\text{MHz}$, we therefore detune the driving frequency of the AOM to $f_{AOM} = 70.125\,\text{MHz}$. Here, $N = 4$, and $M = 561$. Experimental justification for such a choice of sampling frequency is provided in Section 4.1, where the scheme was shown to have been successful.

The sampling can be done by any analogue to digital converter (ADC), at a sampling frequency $f_s = \frac{4}{M}f_{\text{AOM}}$ attached to it.

3.4 From Phase to Relative Length Changes

At this point, the discussion for obtaining the optical phase difference ϕ_d under the scheme of I/Q demodulation is in principle complete. However, the definition of optical phase difference, as given in Equation (2.1), may falsely elude that the problem of determining the relative length changes ΔL is also in principle well-determined, when it is not. A hint as to why this is the case is also found in the reason to the choice of sampling scheme, where phase is a 2π periodic quantity. Specifically, Equation (3.6) yields only the principle value. Formally, the arctangent function $\tan^{-1}$ maps the reals $\mathbb{R}$ to the interval $(-\pi, \pi]$.[1] In other words, the optical phase difference ϕ_d as provided in

$$\phi_d = 2k\Delta L \qquad \in \mathbb{R}, \tag{2.1 modified}$$

$$\phi_d = \tan^{-1}\left(\frac{Q}{I}\right) \qquad \in (-\pi, \pi], \tag{3.6 modified}$$

are not the same.

Therefore, we have to "unwrap" the measured phase to obtain the relative length changes ΔL, which is certainly a quantity much larger than π/k.

As prior asserted in Chapter 2, we expect some change in the optical phase difference ϕ_d over time. Hence, it is sensible to view the complex phasor as having I, Q **coordinate** at time t_i as given by $(I_i, Q_i) = (y_i, y_{i+1})$. However, this would mean that we are measuring the absolute phase as the phasor walks along the complex circle, instead of the "phase offset" φ_0 associated with "$t = 0$", which slightly differs from the previous section. This view of the I, Q components as coordinates is introduced here to be consistent with Chapter 5.

[1] This convention is chosen to be in line with ISO/IEC 9899:1999.

When viewing the phasor as having coordinate (I_i, Q_i), by this sampling scheme, we expect a $\pi/2$ walk along the complex circle of identical radius after each sample. This gives successive absolute phase ϕ measurements $\phi_0, \phi_1, \phi_2, \cdots \in (-\pi, \pi]$ associated with time $t_0, t_1, t_2, \cdots$, where we expect

$$\phi_{i+1} - \phi_i \approx \frac{\pi}{2} \tag{3.7}$$

if the measured phase was not constrained to the interval $(-\pi, \pi]$. However, since the measured phase is constrained, we can make an educated guess that

$$\phi_{i+1} - \left(\phi_i + \frac{\pi}{2}\right) \approx \begin{cases} -2\pi & \text{if } \phi_{i+1} \text{ “crosses above” } \pi, \\ 0 & \text{if } \phi_{i+1} \text{ does not “cross above” } \pi. \end{cases}$$

Pictorially, we express this intuition as the Figure 3.7.

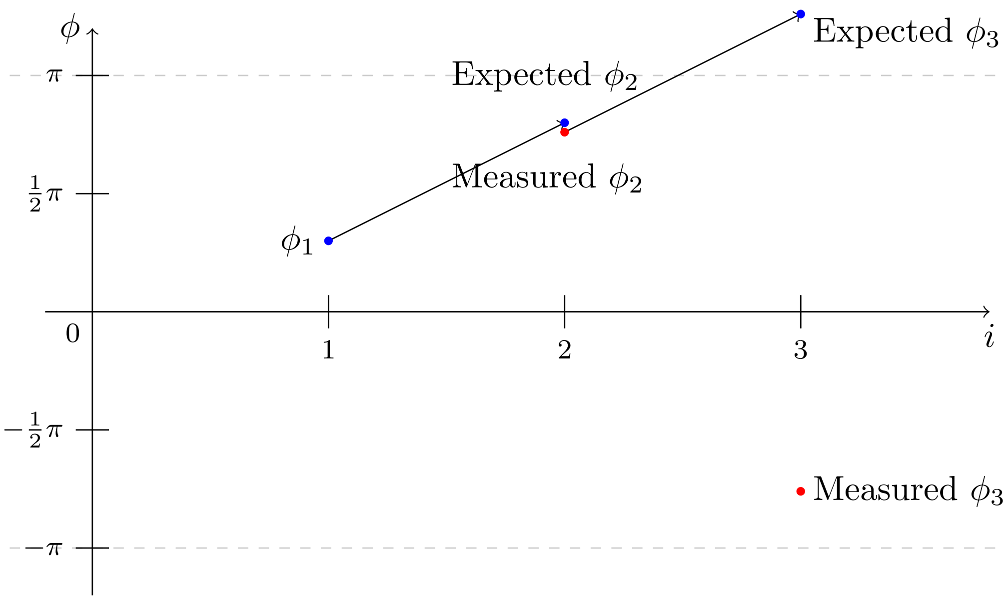

Figure 3.7: Pictorial demonstration of unwrapping 2π periodicity. Blue dots represent phase if there is no relative length changes, while red dots show the phase obtained from $\tan^{-1}$.

Accounting for relative length changes ΔL_i between time t_i and time t_{i+1} that leads to phase difference $\Delta\phi_i$, one can explicitly write as

$$(\phi_{i+1} - \Delta\phi_i) - \left(\phi_i + \frac{\pi}{2}\right) = \begin{cases} -2\pi & \text{if } \phi_{i+1} \text{ “crosses above” } \pi, \\ 0 & \text{if } \phi_{i+1} \text{ does not “cross above” } \pi. \end{cases} \tag{3.8}$$

Rewriting $\Delta\phi_i$ as the subject, we can say that a relative length change (as measured through $\Delta\phi_i$) between time t_i and t_{i+1} to be

$$\Delta\phi_i = \begin{cases} \phi_{i+1} - \phi_i - \frac{\pi}{2} & \text{if} \quad \left|\phi_{i+1} - \phi_i - \frac{\pi}{2}\right| < \left|\phi_{i+1} - \phi_i - \frac{\pi}{2} + 2\pi\right|, \\ \phi_{i+1} - \phi_i - \frac{\pi}{2} + 2\pi & \text{else.} \end{cases} \tag{3.9}$$

Combining everything together, we get the phase differential over time to be

$$\phi_d\left(t_{i+1}\right) = \phi_0 + \sum_{n=0}^{i} \Delta\phi_n, \tag{3.10}$$

and the issue in measuring relative length changes, as presented with the Fibre-base Michelson Interferometer is in principle nullified.

Choice of f_s Nonetheless, it remains clear that the choice of sampling frequency f_s still needs to be frequent enough, such that $\phi_{i+1} - \phi_i$ is reasonably small. By the sampling scheme, it is also clear that the setup cannot distinguish very large length changes such that $\phi_{i+1} - \phi_i \gtrsim 2\pi$ from small length changes; and the choice of sampling frequency should account for perturbations one would expect.

Optimisations Due to the nature of computer code, the use of conditional operators (i.e.: `if ... else ...`) severely slows down the rate of processing. A derivation by observation is done in Appendix A.1, and Equation (3.9) can instead be written as

$$\Delta\phi_i = \left(\phi_{i+1} - \phi_i - \frac{\pi}{2}\right) + 2\pi\, H\left(\pi + \phi_{i+1} - \phi_i - \frac{\pi}{2}\right). \tag{A.1}$$

Chapter 4

I/Q Demodulation Results

With a scheme laid out in the previous chapter to obtain the optical phase difference ϕ_d from the power that exits the phasemeter

$$P_{\text{out}}(t) = \frac{P_{\text{in}}}{2}\left[1 + \cos\left(2\Omega t + \phi_d\right)\right], \tag{3.2}$$

we proceed to test if the proposed scheme is able to perform as expected.

4.1 Initial Proof of Concept

An immediately obvious test one can perform, is to 'knock' near the phasemeter setup gently. The phasemeter output was connected to a photodiode. The photodiode output signal is then connected to an oscilloscope sampling at 100 kS/s. Meanwhile, the AOM is driven with a frequency $f_{\text{AOM}} = 80.0125$ MHz.

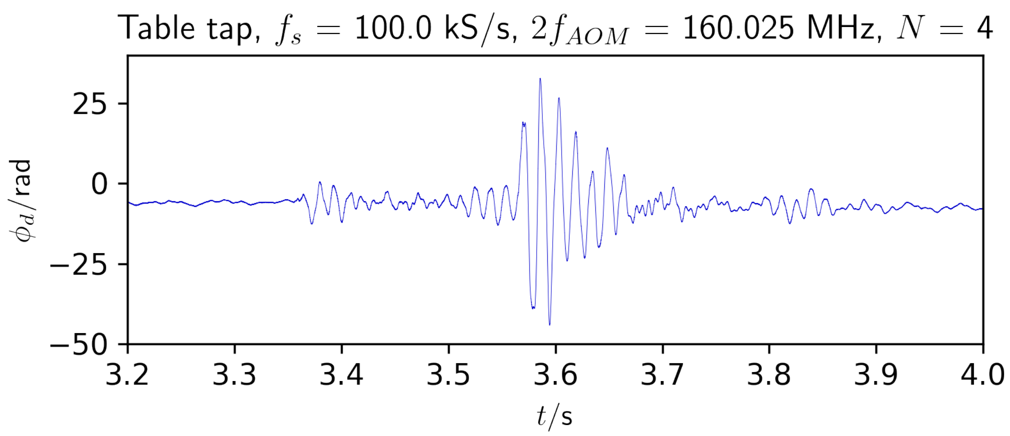

Figure 4.1: A plot of ϕ_d over time, from a period of relative quiet to signal picked up from tapping the table. A distinct ringdown and an envelope can be seen.

After the oscilloscope was set to record, I tapped the table which the phasemeter setup was on, and processed the data in accordance with the scheme described in the previous chapter. The result is shown in Figure 4.1. The strength of the tap is approximately comparable to typing on a keyboard.

The distinct ringdown and fairly clear resolution of the demodulated signal by the scheme presented in Section 3.3 is an indication that the scheme is successful. Furthermore, the relatively low sampling frequency $f_s = 100\,\text{kS/s}$ in contrast to the carrier signal frequency $f = 2f_{\text{AOM}} = 160.025\,\text{MHz}$, is indicative that the proposal for a lower sampling frequency in Section 3.3 is valid.

4.2 Linearity of Response

The Riesz-Fischer theorem [20, 21] states that any *finite time* signal can be represented by a Fourier series. As such, if the phasemeter, along with the demodulation scheme, is able to accurately determine any sinusoidal relative length changes ΔL, it is reasonable to claim that the setup is able to detect all such signals.

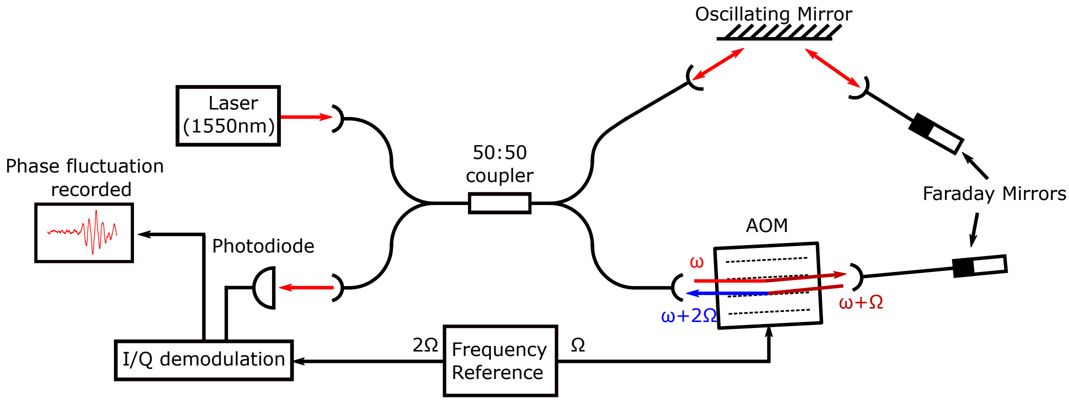

Figure 4.2: Phasemeter was modified with a mirror on a piezoelectric stack to vary ΔL.

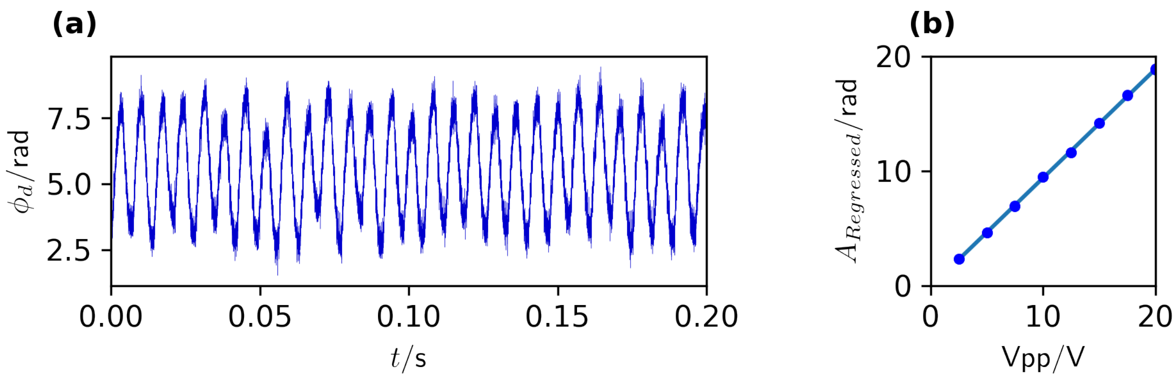

(a) The piezoelectric stack was set to oscillate at $f_{\text{mirror}} = 143\,\text{Hz}$, and sampling frequency $f_s = 1.0\,\text{MS/s}$, with carrier frequency $f = 2f_{\text{AOM}} = 160.25\,\text{MHz}$, $N = 4$.

(b) Linearity of amplitude A of ϕ_d with respect to increased Vpp applied to piezoelectric stack.

Figure 4.3: Figure (a) shows the optical phase difference ϕ_d measured with a peak to peak voltage of 2.5 V applied to the piezoelectric stack. Figure (b) shows the linear regression of obtained amplitudes A for measured ϕ_d with different peak to peak driving voltages to the piezoelectric stack.

To do so, a mirror attached to a piezoelectric stack was placed in the path of one arm of the phasemeter, as shown in Figure 4.2. This allows us to modulate the relative length differences ΔL in the two arms of the phasemeter in a controlled manner.

A relatively low oscillation frequency was then set, and the resulting ϕ_d was obtained and regressed against a sinusoidal function. The obtained ϕ_d was then compared against the input into the piezoelectric.

In Figure 4.3, an example of obtained ϕ_d over 200 ms is shown in Figure 4.3a for the specified setting. A sinusoidal voltage with 2.5 peak to peak voltage at 143 Hz was applied to the piezoelectric stack. A sinusoidal regression was then performed against ϕ_d, and the amplitude A was recorded. The regression of A against the various peak to peak voltages were then performed, as shown in Figure 4.3b. The error bars are too small to be seen in the figure. The linearity is therefore observed.

The same measurement was then repeated with different oscillation frequencies, and all were also found to be linear. However, the gradients m in the regression were found to decrease with increased frequency of oscillation, but this was likely due to a decreasing responsiveness of the piezoelectric stack.

4.3 Complications

In the previous cases, a peculiar phenomenon was increasingly observed that could not be attributed to merely a fluke of data collection.

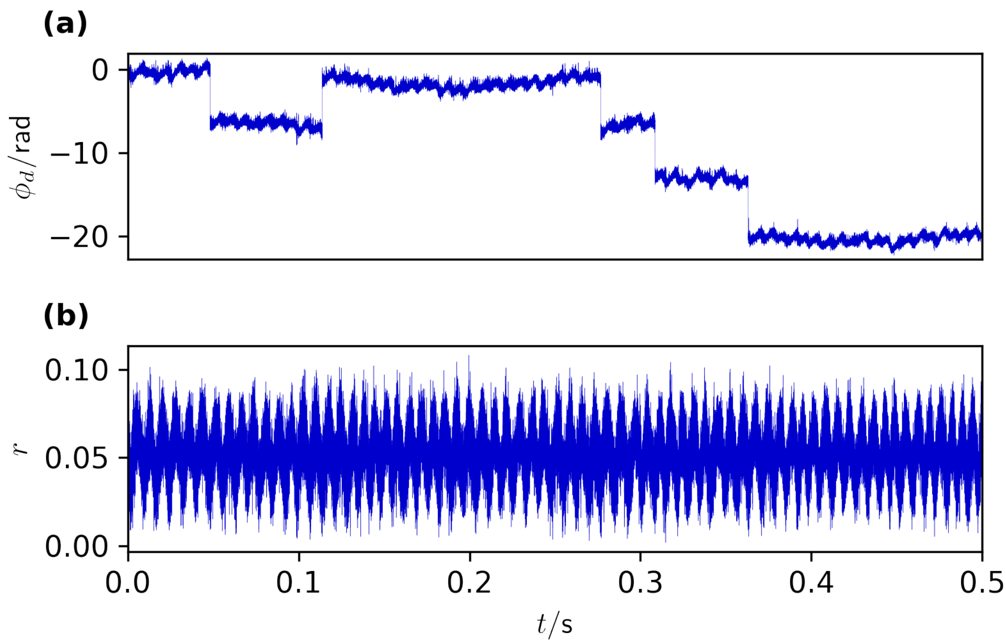

Figure 4.4: A plot of (a) ϕ_d, and (b) its corresponding radius r in the I/Q-plane. This mirror oscillation was set at 1.02 V and 4.0 Hz. f_s =1.0 MHz, f_{AOM} = 80.125 MHz.

Figure 4.4a is a typically observed ϕ_d collected when using a short optical fibre. Looking closer, it is clear that the optical phase ϕ_d obtained was not natural; where the envelope of the optical phase appears to have 'jumped' by approximately 2π rad.

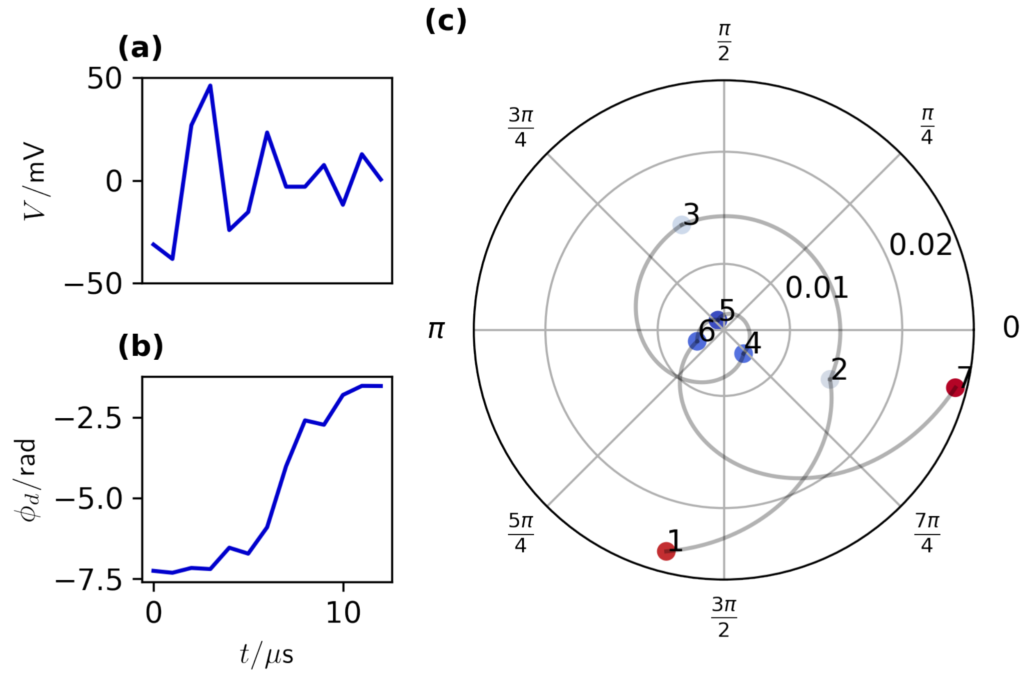

Figure 4.5: A closer look into the increasing 2π jump of Figure 4.4. Figure (a) and (b) provides the recorded voltage and unwrapped ϕ_d around the 2π jump. Figure (c) provides a plot of the individual (I, Q) coordinates around the occurrence of the 2π jump. Looking at points 5 and 6, it is clear that the expected phase advance of $\pi/2$ did not occur, therefore contributing to a jump.

Error Correction Whilst investigating the reason for these jumps, a fast[1] algorithm was created to correct them.

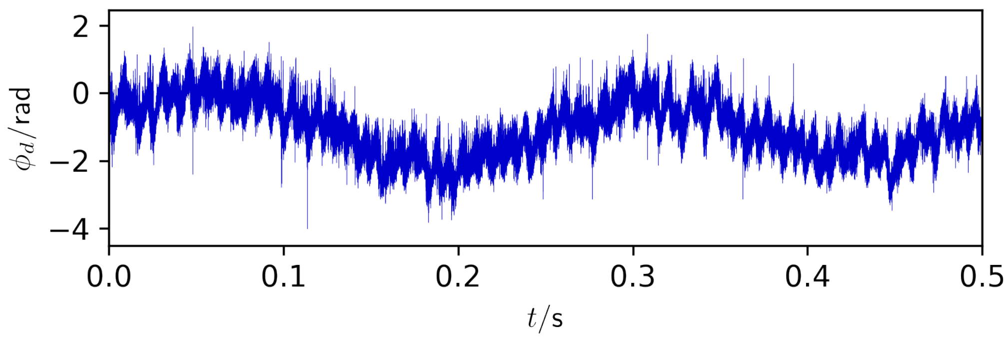

Figure 4.6: The error correction algorithm as described in Appendix B as applied to Figure 4.4a. The envelope appears fairly continuous, which indicates that it is indeed a jump.

The outcome of the algorithm had definitively shown that these were indeed 2π jumps, and that the envelope was indeed continuous after utilising the algorithm. As the algorithm detracts from the discussion here, it has been left for in the Appendix B. Figure 4.6 shows that the envelope is indeed continuous, and that it is therefore accurate to call these a jump.

However, we take special note that identifying the hyperparameters necessary to perform

[1] The algorithm runs in $O(n)$ time, where n is the number of ϕ_d points sampled

the algorithm ideally is not a trivial matter, and that further investigation into the physical source of these jumps were necessary.

Physical Sources of 2π jumps Diving deeper into the data that was collected that had produced ϕ_d in Figure 4.4a, was the start of investigating the source of these jumps. Initially, I had made a plot of the (I, Q) coordinates around the jump as given in Figure 4.5c. Figure 4.5a, and b, are the plots of the sampled voltage V and optical phase differences ϕ_d around the jump. With the (I, Q) coordinates plotted, it immediately became apparent that studying just the phase, and not the radius does not paint a complete picture. This is further exemplified in Figure 4.4b, which was made with hindsight. Here, the collected data shows that the assumptions in the scheme that

1. Radius of (I, Q) coordinates is fairly constant, and
2. Expected phase 'advancement' between consecutive points being $\pi/2$

were not necessarily true. As such, Figure 4.4b was made in hindsight, and it can be seen that the radius component of (I, Q), i.e.: $r = \sqrt{I^2 + Q^2}$ oscillates regularly, with values almost approaching zero.

Furthermore, using a spectrum analyzer at the photodiode signal did not reveal much that was unusual either.

The most probable explanation is that the radius approaching 0 is the source for jumps, but it still remains unclear why this would be the case.

Increasing sampling frequency One might consider that increasing the sampling frequency means that the difference between two consecutive optical phase difference ϕ_i and ϕ_{i+1} might be smaller, and therefore, the chance of a 2π jump occurring is less.

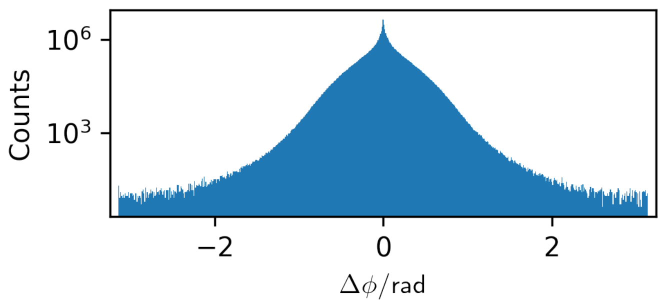

Figure 4.7: Histogram of consecutive optical phase difference $\Delta\phi_d$ for $f_s = 1.0\,\text{MHz}$, over 50 seconds.

f_s / MHz	Std. Dev.
0.10	0.283
0.25	0.234
0.50	0.235
1.00	0.216
2.50	0.202
10.0	0.191

Table 4.1: Standard deviation of the distributions of $\Delta\phi_d$ obtained for each sampled frequency f_s.

Using a 130 m optical fibre, and several sampling frequencies, the histogram of difference in optical phase difference $\Delta\phi_i = \phi_{i+1} - \phi_i$ was identified. An example for the case of 1 MHz is as shown in Figure 4.7. The results of the standard deviation for the various sampling frequencies is as shown in the corresponding table. The optical phase difference ϕ_d to Figure 4.7 is shown in Figure 4.9.

While the standard deviation does decrease with increased sampling frequency, the number of samples per unit time does increase with sampling frequency. Another important point to note is that there is a sizeable number of $\Delta\phi_i$ that is almost at $\pm\pi$, which indicates numerous 2π jumps. This persists even at 10 MHz sampling frequency.

Uncertainty evaluation One may consider thinking of the (I, Q) coordinates as having some associated uncertainty, thereby instead allowing us to think of the coordinate as a distribution centered at some point with the average radius. The measured coordinates (I, Q) is then some randomly chosen point in the distribution.

However, the radius oscillating with such regularity as exemplified in Figure 4.4b, is not a behaviour of noise, and such a consideration is to be ruled out.

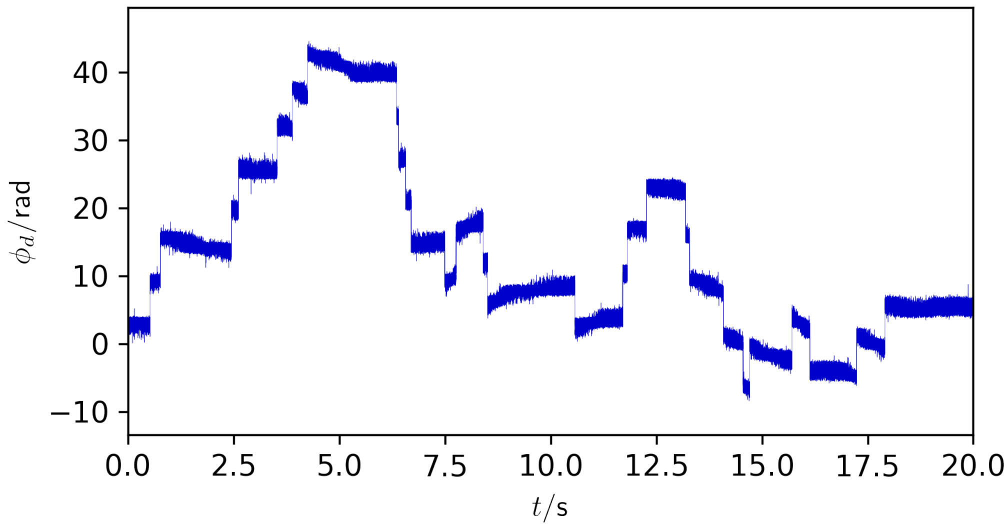

Figure 4.8: Using a 130 m optical fibre instead, the demodulated optical phase difference ϕ_d starts to exhibit a random walk instead. $f_s = 1.0\,\text{MHz}$, $f_{\text{AOM}} = 70.125\,\text{MHz}$.

Necessity for better methods of extracting phase Repeating the same process to obtain ϕ_d, but now for a much longer optical fibre of 130 m in the absence of the oscillating mirror, the result is as shown in Figure 4.8 and 4.9. Here, we can see the extent of 2π jumps resemble a form of random walk, which one might have wrongly assumed as a walk in the optical fibre length, if not for the backdrop of information established up to this point.

Tuning the algorithm as described in Appendix B to correct such a random walk is unfeasible, and that a better physical sampling scheme is preferential. A better method is instead proposed in the next chapter, Chapter 5.

The next section is an attempt to try further explain the source of these jumps through the use of a mathematical model.

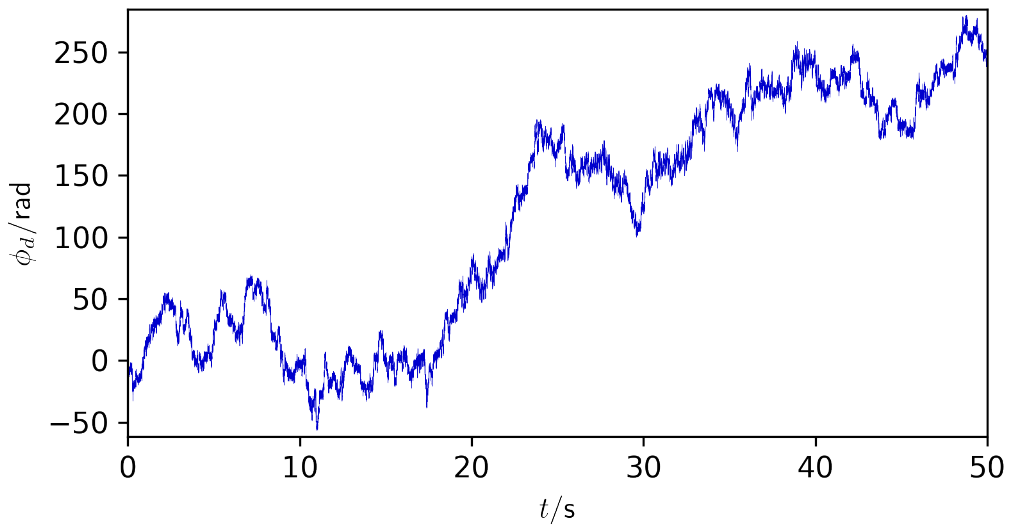

Figure 4.9: A more extreme example of an experimentally observed random walk. $f_s = 1.0\,\mathrm{MHz}$, $f_{\mathrm{AOM}} = 70.125\,\mathrm{MHz}$.

4.4 Mathematical Modeling

Consider the voltage that is emitted from the photodiode (as in Figure 4.2) to be of the form

$$V(t) = V_0 \sin(2\Omega t + \phi_1 + A \sin(2\pi f_{\mathrm{Mirror}} t + \phi_2) + \mathcal{L}) + \mathcal{D}. \tag{4.1}$$

Here, $\mathcal{L}, \mathcal{D}$ denote noise terms in the length of the optical fibre, and 'detector' respectively.

As a toy model, consider that the fibre length noise and detector noise are that of a Gaussian noise at every time step sampled, i.e.: $\mathcal{L} = L\mathcal{N}\left(0, {\sigma_1}^2\right)$, and $\mathcal{D} = D\mathcal{N}\left(0, {\sigma_2}^2\right)$; where L, D are coupling strengths, and $\mathcal{N}\left(0, {\sigma_i}^2\right)$ is the normal (Gaussian) random variable with some variance ${\sigma_i}^2$ centered at 0.

In an attempt to replicate Figure 4.4 and the signal $V(t)$ that was sampled to create it, V_0 was set to 0.092, and L was arbitrarily set to a relatively small value of 0.020, with $\sigma_2 = 0.3$. Then, the value of L, σ_1 was slowly increased from 0, and the corresponding $\phi_d(t)$ was then observed as shown in Figure 4.10.

If we treat the oscillating mirror $A \sin(2\pi f_{\mathrm{Mirror}} t)$ as the deterministic component of changes in the fibre length, and $\mathcal{L}$ as the noise component of changes in the fibre length; it was found that for fixed small L, σ_1, a small value in A (i.e.: some deterministic change in the fibre length) was also necessary for 2π jumps to occur.

This toy model has therefore shown that deterministic changes in fibre length over time $\Delta L(t)$, together with sufficiently noisy changes in the fibre length $\mathcal{L}$, along with a small amount of detector noise would have created 2π jumps.

Possible Improvements We first introduce the concept of power spectral density. The spectral density function[17] S of frequency f (in Hertz) for a stationary signal $x(t)$ measured

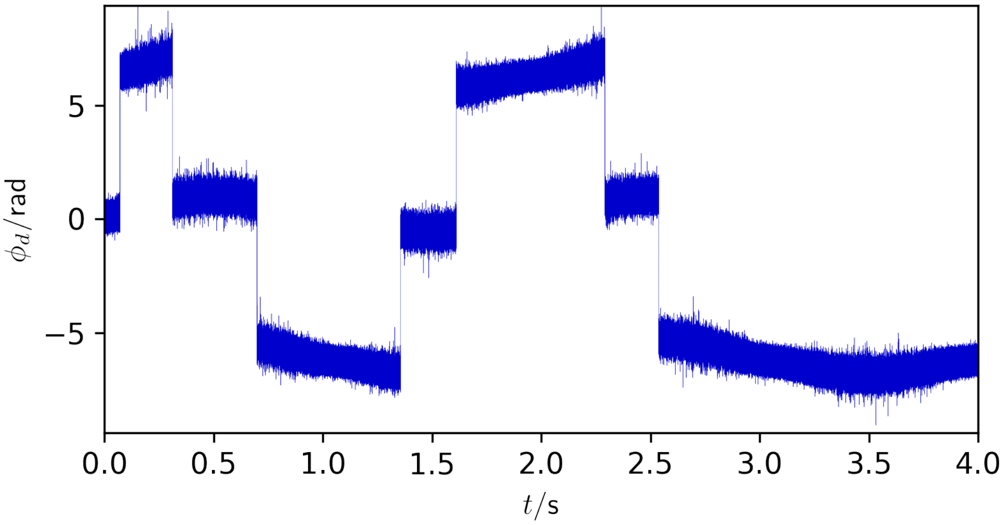

Figure 4.10: 2π jumps observed using the toy model. $V_0 = 0.092$, $A = 0.8$, $f_{\mathrm{Mirror}} = 0.5\,\mathrm{Hz}$, $L = 1$, $\sigma_1 = 0.48$, $D = 0.020$, $\sigma = 0.3$, $f_s = 1.0\,\mathrm{MHz}$, $f_{\mathrm{AOM}} = 70.125\,\mathrm{MHz}$

over a finite time T, is given by

$$S(f) = \frac{2}{T}\left|\int_{-T/2}^{T/2} x(t)e^{-i2\pi ft}\,\mathrm{d}t\right|^2 \tag{4.2}$$

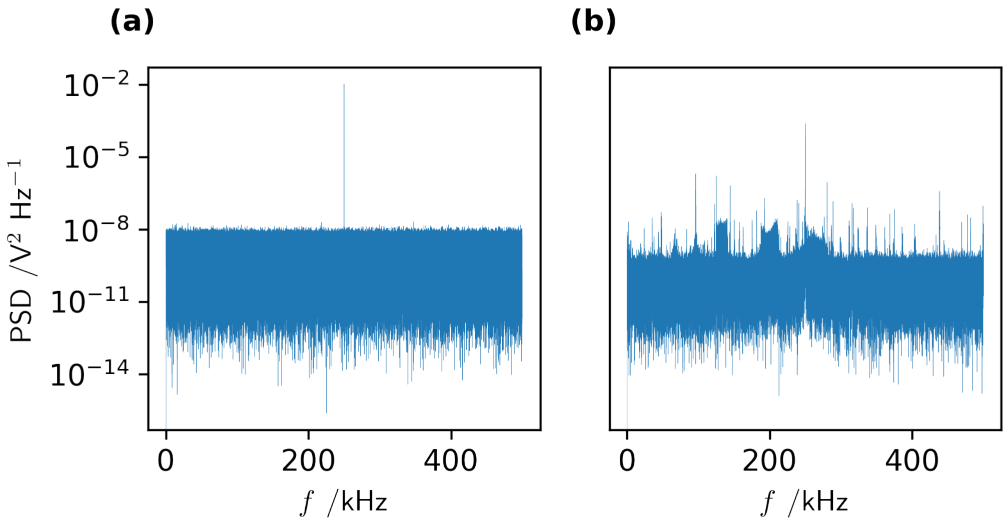

Figure 4.11: Figure (a) is the power spectrum density (PSD) of the signal $V(t)$ as provided in the toy model to Figure 4.10. Figure (b) is the power spectrum density of the signal $V(t)$ that was sampled to have produced Figure 4.4.

Experimentally, the power spectral density of the signal that produced Figure 4.4 is shown in Figure 4.11b with a distinct peak at 250 kHz. This peak of 250 kHz is expected, as it is identically $2f_{\mathrm{AOM}} \mod f_s$, which is the frequency at which the phase advance $\pi/4$ is expected to evolve. Note that the toy model demonstrates a distinctly white noise spectrum, whilst the real signal deviates from a white noise spectrum, and therefore, likely to have different properties from which the toy model does not exhibit.

We however note that, the goal of this mathematical toy model is not to completely replicate the experimental data, but to give insight as to its reason for occurrence.

For the situation of the random walk as presented in Figure 4.9, one might instead consider a different noise model, such as the Weiner process [22] to model the noise terms $\mathcal{L}$. The corresponding power spectrum density for the modeled $V(t)$ will be different, but does not come anywhere close to the power spectrum density of the real data.

Chapter 5

Non-I/Q Demodulation

Having no good physical reason as to the source of 2π jumps as discussed in Section 4.3, a different approach is required.

In this chapter, we will rework some of the machinery that has been discussed in Section 3.3 but using points along the sinusoidal that are not $\pi/2\,\mathrm{rad}$ apart, but with any arbitary value. This still allows for the identification of phase information of the carrier signal. This is termed as "Non-I/Q demodulation".[19] Thereafter, this chapter will discussed the optical phase difference ϕ_d obtained by non-I/Q demodulation, in contrast to the results of Chapter 4.

5.1 Digital Non-I/Q Demodulation

In Section 3.3, we stated that

$$y = \underbrace{A\cos\varphi_0}_{I}\sin\omega t + \underbrace{A\sin\varphi_0}_{Q}\cos\omega t. \tag{3.5}$$

Let us instead now consider measuring at times t such that ωt is multiples of some θ that is a rational fraction of 2π. This gives successive samples y_j measured to be[19]

$$j \in \{0, 1, \cdots, N-1\}, \quad y_j = I\cdot\sin(j\theta) + Q\cdot\cos(j\theta). \tag{5.1}$$

The value of N will be further elaborated later. In the case of ideal sampling without noise,

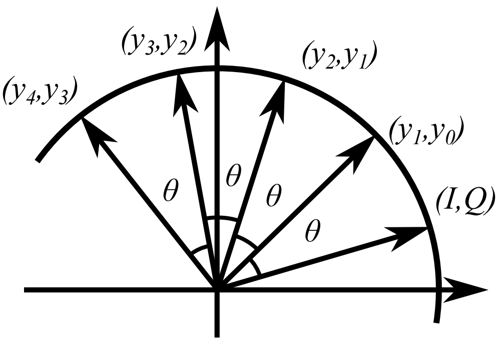

Figure 5.1: Phasor in I/Q plane advancing by arbitary angle θ.

any 2 equations from Equation (5.1) would give a solution to I, Q; but a different method is required in the presence of real conditions.

Regression To obtain the appropriate values of I, Q, one can apply an unbiased estimator for the least mean squares algorithm.[23] We aim to minimize the function[19]

$$f(I, Q) = \sum_{j=0}^{N-1} \left[I \cdot \sin(j\theta) + Q \cdot \cos(j\theta) - y_j \right], \tag{5.2}$$

where y_j is the j^{th} sampled value along the sinusoidal $y(t_j)$. The minimization is given by[19]

$$\frac{\partial f}{\partial I} = 0, \qquad \frac{\partial f}{\partial Q} = 0. \tag{5.3}$$

Solving these would then give[19]

$$I = \frac{2}{N} \sum_{j=0}^{N-1} y_j \cdot \sin(j\theta), \tag{5.4a}$$

$$Q = \frac{2}{N} \sum_{j=0}^{N-1} y_j \cdot \cos(j\theta), \tag{5.4b}$$

which are the (I, Q) coordinates of the 0^{th} sampled point y_0. We can repeat the same for the next data point y_1, getting a different (I, Q) coordinate, with an expected phase advance of θ.[19]

5.2 Sampling and Carrier Frequency

This section clarifies on the values N and θ from the previous section.

Similar to Section 3.3, consider any sampling frequency f_s and carrier frequency $f = \omega/2\pi$,

$$f_s = \frac{N}{M} f, \tag{5.5}$$

but now only with requirement that N/M is positive rational $\mathbb{Q}_{>0}$.[19] Interpreting in the time domain, this means that N samples are taken in M consecutive carrier periods, such that the phasor returns to its initial position, modulo 2π. This gives the phase advance to be

$$\theta = \frac{M}{N} \cdot 2\pi \mod 2\pi. \tag{5.6}$$

We take care to note that while we might not care too much for the value of M, as discussed in Section 3.3, it is a logical fallacy to deduce the value of θ directly from the value N. For example, $N = 8$ does not imply that $\theta = \pi/4$, as $\theta = 3\pi/4$, $5\pi/4$, $7\pi/4$ are equally valid as a solution.

For integer f_s and f, the values of N, M are given very simply by

$$N = \frac{1}{\gcd(f_s, f)} f_s, \tag{5.7a}$$

$$M = \frac{1}{\gcd(f_s, f)} f, \tag{5.7b}$$

where $\gcd(\cdot,\cdot)$ is the greatest common divisor operator.

Phase Unwrapping Generalising from Section 3.4, with more detail in Appendix A.1, the relative length change (as measured through $\Delta\phi_i$) between time t_i and t_{i+1} is then

$$\Delta\phi_i = \begin{cases} (\phi_{i+1} - \phi_i - \theta) + 2\pi\, H(\pi + \phi_{i+1} - \phi_i - \theta), & \text{for } \theta \in (0, \pi), \quad \text{(A.1)} \\ (\phi_{i+1} - \phi_i - \theta) - 2\pi\, H(-\pi + \phi_{i+1} - \phi_i - \theta), & \text{for } \theta \in (-\pi, 0). \quad \text{(A.4)} \end{cases}$$

Sampling Scheme For this chapter, we chose to work with $N = 8$, and $\theta = \pi/4$. This is done by setting the sampling frequency to 1.0 MHz and Ω to 70.0625 MHz, unless otherwise specified. This is therefore, an advantage of this experimental setup, as one can very easily utilise such a different sampling scheme.

In principle, one could choose any integer for N, such as $N = 5$. However, the produced the optical phase difference ϕ_d was not sensible, and it was suspected that powers of 2 would only work. This has however, not been verified for $N = 16, 32, \cdots$.

5.3 Test of Concept and Resiliency Comparison

In the many repeated tests with the new scheme, no 2π jumps were initially noticed over the case of sampling in 1 s intervals. This was a significant improvement over the $N = 4$ sampling scheme. Figure 5.2 shows ϕ_d without deliberately generated noise, in direct comparison against Figure 4.8.

Looking closer at Figure 5.2, the envelope to the optical phase difference ϕ_d appears to vary much less than Figure 4.8. To further substantiate that the 2π jumps are correlated with the radius approaching 0, we note that in Figure 5.2, the radius over the entire 20 s was measured to be 0.114(14); whereas the radius over the 20 s in Figure 4.4 was measured to be 0.122(19). The decrease in standard deviation from 0.019 to 0.014 under identical physical setup, in similar noise conditions when taking $N = 4 \to 8$ means that the likelihood that it is very near 0 is much less. Both data sets were taken back to back. Therefore, jumps being related with low r values is further substantiated. Furthermore, we show that increasing the value of N from 4 to 8 is better at providing physically sensible optical phase difference ϕ_d.

Taking a smaller time segment, the radius of Figure 4.8 and 5.2 is shown in Figure 5.3. One can observe the extent of this difference in standard deviation, even if the numerical difference is approximately 30%.

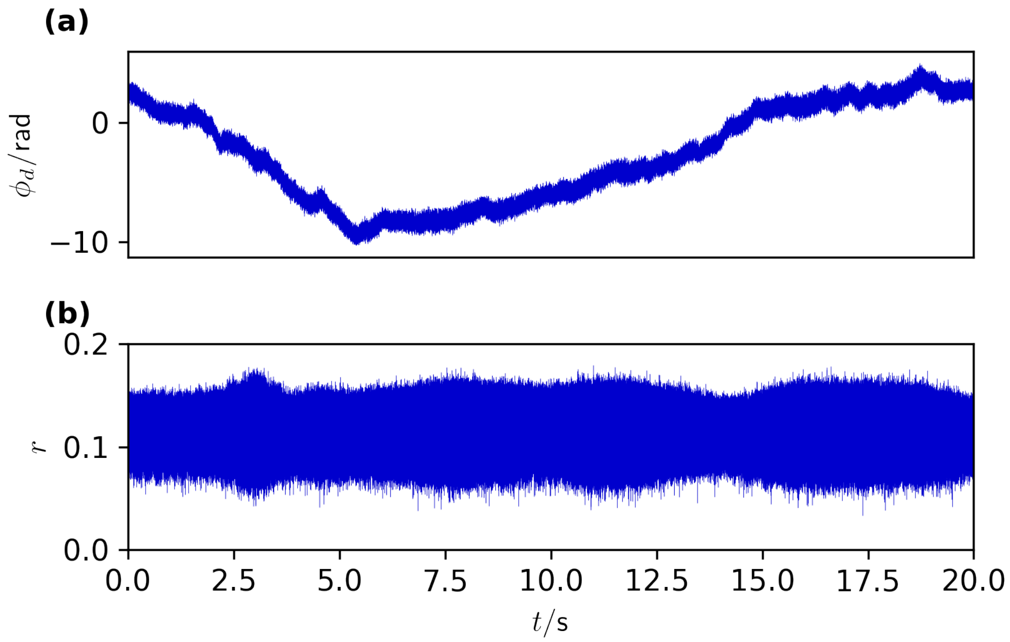

Figure 5.2: A plot of (a) ϕ_d, and (b) its corresponding radius r in the I/Q-plane. This was sampled without deliberate perturbation. $f_s = 1.0\,\text{MHz}$, $f_{\text{AOM}} = 70.0625\,\text{MHz}$.

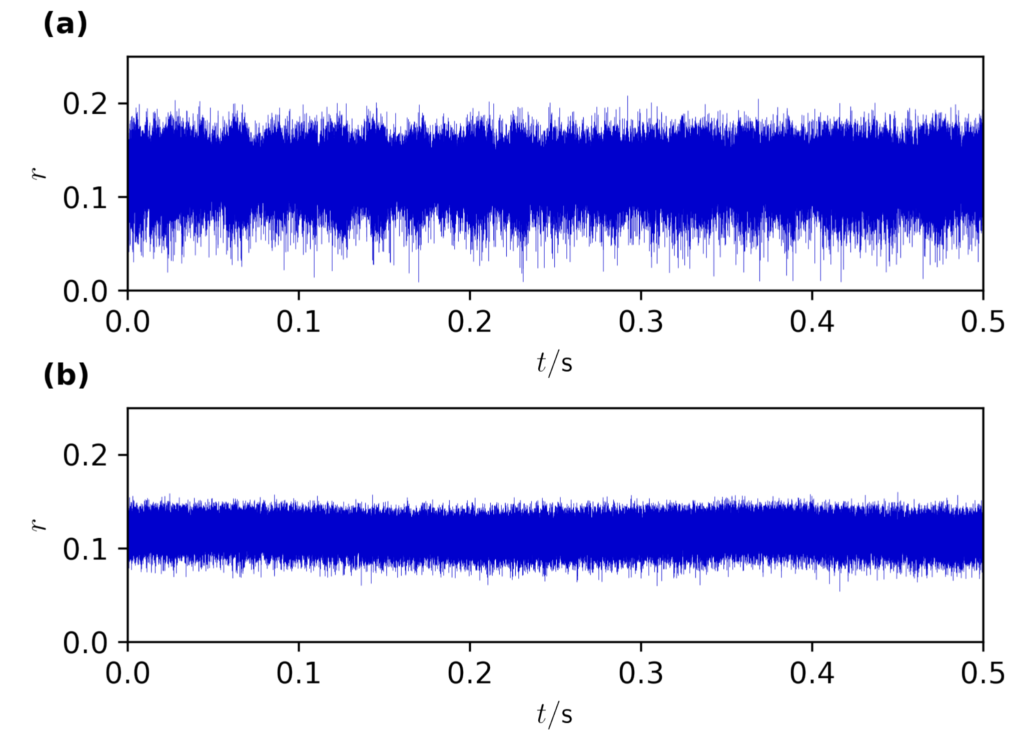

Figure 5.3: A smaller time slice of the radius r in the I/Q-plane from Figure 4.8 and Figure 5.2 respectively.

5.4 Perturbation Sensing in the Lab

One would expect that the extent of human activity to be significantly less at night than in the day. Due to the limitation of the existing setup, continuous recording of data is at present still not feasible. As such, we opted for the next best option, to record the voltage $V(t)$ as frequently as possible. As an initial run, we settled for the sampling 1 s of data every 61 s.

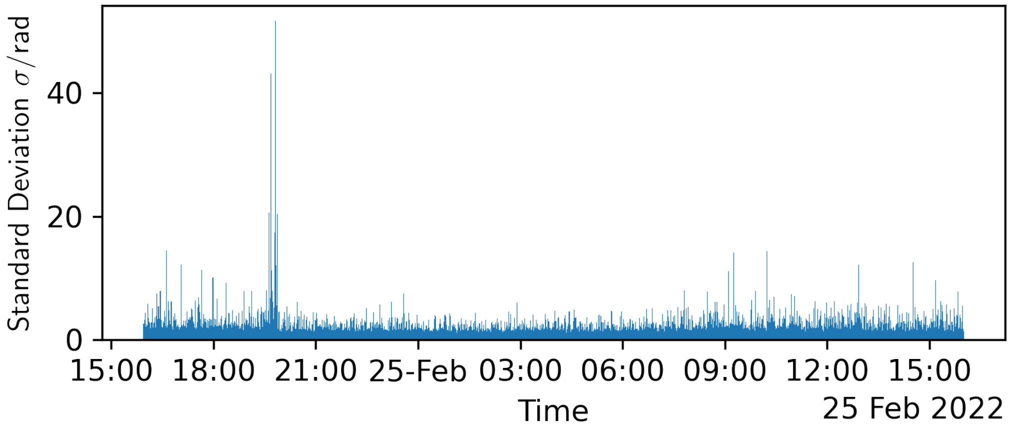

Figure 5.4: Standard deviation σ of $\phi_d(t)$ over the course of one second, per 61 second interval. This was started on 24 February 2022, and was left to run for about a day. This is a proxy for the measure of human activity within the lab.

After collecting the data for approximately a day, starting from 24$^{\text{th}}$ February 2022 15:57 pm, the optical phase difference ϕ_d for each time segment was then obtained, and the standard deviation σ over the entire of $\phi_d(t)$ for the one-second interval, was obtained. The result is shown in Figure 5.4.

Comparing day against night, it is clear that the noise observed during lab hours is larger than that of at night, where people are not around in the lab, and the data conforms with our expectations.

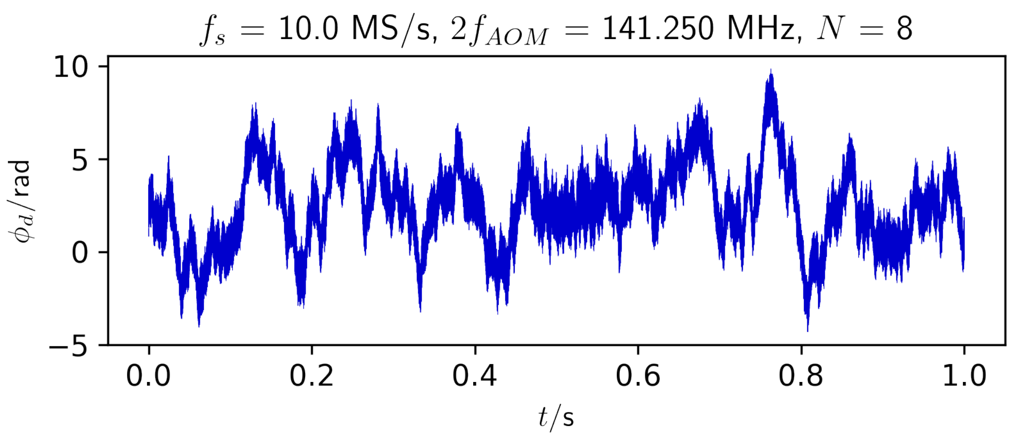

Figure 5.5: ϕ_d obtained at 5pm. This is one of the many samples taken over the course of the day.

5.5 Toy Model

With reference to Section 4.4, Figure 4.10, we can replicate the mathematical modelling under identical noise conditions, but under the scheme of non-I/Q demodulation. With all values kept constant except for $f_{\mathrm{AOM}} = 70.0625\,\mathrm{MHz}$, the obtained ϕ_d is as shown in Figure 5.6.

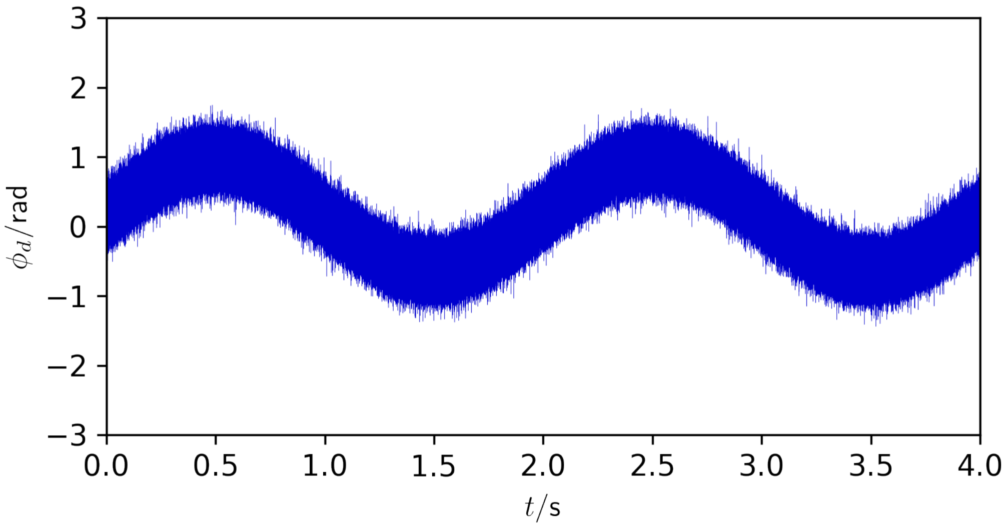

Figure 5.6: 2π jumps observed using the toy model. $V_0 = 0.092$, $A = 0.8$, $f_{\mathrm{Mirror}} = 0.5\,\mathrm{Hz}$, $L = 1$, $\sigma_1 = 0.48$, $D = 0.020$, $\sigma = 0.3$, $f_s = 1.0\,\mathrm{MHz}$, $f_{\mathrm{AOM}} = 70.0625\,\mathrm{MHz}$

This further supports the robustness of $N = 8$ non-I/Q demodulation, in contrast to the case of $N = 4$ for I/Q demodulation.

Chapter 6

Summary

This thesis, first demonstrates the modification of a typical fibre-based Michelson interferometer into a heterodyned phasemeter. Several properties of our experimental setup was then characterised, before the I/Q demodulation scheme was described. This I/Q demodulation scheme allows for the digital sampling of data from the phasemeter to determine the directional displacement in the optical path difference between the two arms of the interferometer.

With the I/Q demodulation scheme, experimental results were collected and analysed, but an issue with jumps was soon found. Work was then placed into the correction, and identification of the source of this jumps, but no good physical reason could be found.

As an advantage of the experimental setup, non-I/Q demodulation was explored, and the results proved successful in contrast to I/Q demodulation.

Appendix A

Optimisations

A.1 Phase "unfolding"

In Chapter 3.4, the "unfolding" of measured absolute phase $\phi_i \in (-\pi, \pi]$ to optical phase difference $\phi_d \in \mathbb{R}$ was shown. For ease of reference, the key equations are repeated here:

$$\phi_{i+1} - \phi_i \approx \frac{\pi}{2} \tag{3.7}$$

$$\Delta\phi_i = \begin{cases} \phi_{i+1} - \phi_i - \frac{\pi}{2} & \text{if} \quad \left|\phi_{i+1} - \phi_i - \frac{\pi}{2}\right| < \left|\phi_{i+1} - \phi_i - \frac{\pi}{2} + 2\pi\right|, \\ \phi_{i+1} - \phi_i - \frac{\pi}{2} + 2\pi & \text{else.} \end{cases} \tag{3.9}$$

which was said to required optimisation. As further shown in Chapter 5, Equation (3.7) could have instead been any sensible value, such as between 0 and π.

Since $\phi_i \in (-\pi, \pi]$, consider a variable u defined by $\phi_{i+1} - \phi_i \in (-2\pi, 2\pi]$, and variable $\theta \in (0, \pi]$, which plays the role of generalising the $\pi/2$ in Equation (3.7). Studying Equation (3.7) closely, we notice that u and θ always come together, and therefore we define $x = u - \theta \in (-2\pi - \theta, 2\pi - \theta]$.

We utilise a concept in computer science known as branchless programming, where conditional statements such as `if`, `switch` and other conditional statements translates to a `mov` command in Assembly, among other inefficiencies. Removing avoidable branches is therefore a good practice.

This encourages us to define a mathematical function that does not require the use of a 'branch', and with some experimentation, we get the function f defined by

$$\Delta\phi = f(x) = f(u - \theta) = x + 2\pi\, H(\pi + x), \tag{A.1}$$

where $H(x)$ is the Heaviside function. Plotting for fixed values of θ, we get Figure A.1, which behaves as we expect.

That said, while it has not been rigorously tested with the experimental setup, it is not adviseable to choose values of θ too close to π.

The next part is written in context of Section 5.1, where the possible values of θ could be much different. For choices of $\theta \in [\pi, 2\pi)$ (which is equivalent to $\theta \in [-\pi, 0)$ by the 2π periodicity), note that the intuition that led to Equation 3.9 would differ slightly. The phase

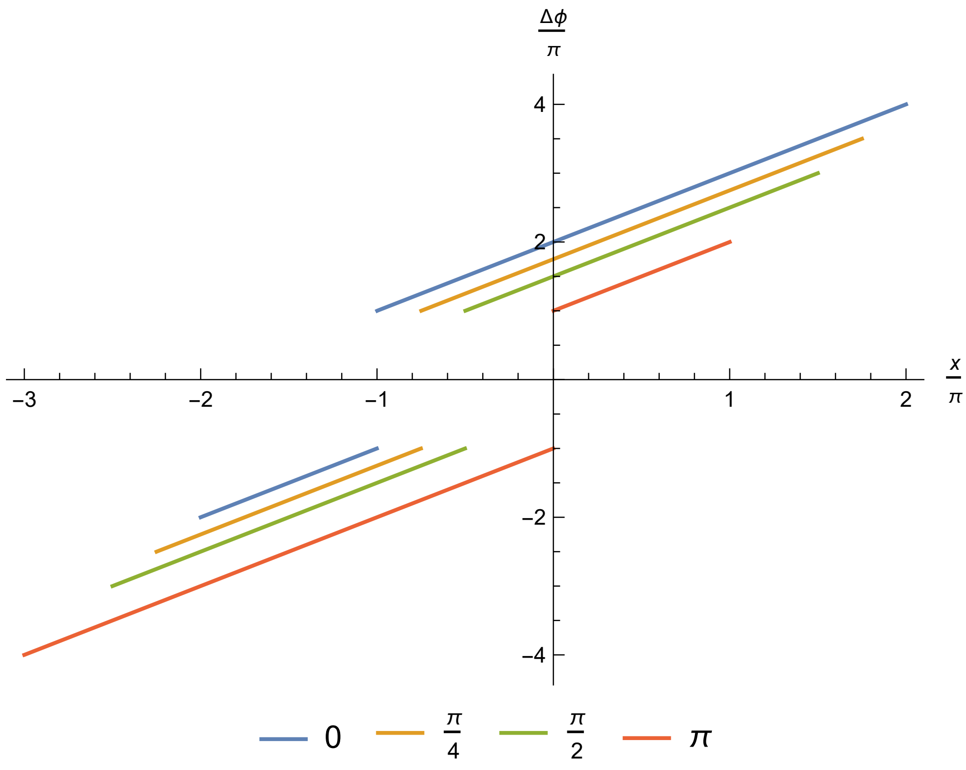

Figure A.1: A plot of expected $\Delta\phi_i$ for various x, with θ fixed to 4 values.

advance would then have one expect that $\Delta\phi < 0$, and the jump as shown in Figure 3.7 would instead be

$$(\phi_{i+1} - \Delta\phi_i) - (\phi_i + \theta) = \begin{cases} 2\pi & \text{if } \phi_{i+1} \text{ “crosses below” } -\pi, \\ 0 & \text{if } \phi_{i+1} \text{ does not “cross below” } -\pi. \end{cases} \tag{A.2}$$

Rewriting $\Delta\phi_i$ as the subject, we can say that a relative length change (as measured through $\Delta\phi_i$) between time t_i and t_{i+1} to be

$$\Delta\phi_i = \begin{cases} \phi_{i+1} - \phi_i - \theta & \text{if } \quad |\phi_{i+1} - \phi_i - \theta| < |\phi_{i+1} - \phi_i - \theta - 2\pi|, \\ \phi_{i+1} - \phi_i - \theta - 2\pi & \text{else.} \end{cases} \tag{A.3}$$

The branchless function f is then written as

$$\Delta\phi = f(x) = f(u - \theta) = x - 2\pi\, H(-\pi + x) \tag{A.4}$$

for $\theta \in [-\pi, 0)$.

A.2 Discrete Convolution

Mathematical Definition For complex-valued functions f, g defined on the set $\mathbb{Z}$ of integers, the discrete convolution of f and g is given by [20]

$$\{f * g\}(n) = \sum_{m\in\mathbb{Z}} f(m)g(n-m) \tag{A.5a}$$

or equivalently

$$\{f * g\}(n) = \sum_{m\in\mathbb{Z}} f(n-m)g(m). \tag{A.5b}$$

Example of Convolution Used in the Project With reference to Section 5.1, the following equations are reproduced here.

$$I = \frac{2}{N}\sum_{j=0}^{N-1} y_j \cdot \sin(j\theta), \tag{5.4a}$$

$$Q = \frac{2}{N}\sum_{j=0}^{N-1} y_j \cdot \cos(j\theta). \tag{5.4b}$$

This is a strong example where convolution is used alot in the project. Utilising a for loop in any high level, interpreted language such as Python would be very slow. Optimising this step to utilise convolutions, which often has native or optimised open-source implementations, would be ideal.

We recall that we wish to determine (I_i, Q_i) for the sampled points y_i, for which there are alot of. Looking closely at the two equations, it looks similar to Equation A.5a with a scale factor, and the domain $\mathbb{Z}$ has been constrained. Properly rewriting for all sampled points y_i and their corresponding (I_i, Q_i) coordinate, we have

$$I_i = \frac{2}{N}\sum_{m=i}^{N-1+i} y_m \cdot \sin((m-i)\,\theta), \tag{A.7}$$

$$Q_i = \frac{2}{N}\sum_{m=i}^{N-1+i} y_m \cdot \cos((m-i)\,\theta). \tag{A.8}$$

This can be easily be written as a convolution, by identifying f with y, and g by

$$i \in \{0, 1, \cdots, N-1\}, \qquad g(i) = \sin((N-1-i)\,\theta),$$

or the cos equivalent to obtain Q. Note that if there are l sampled values of y_i, then the last $N-1$ points do not have their coordinates known. In other words, only $l+1-N$ points will have I, Q coordinates known.

Example in Python Using numpy `np`, we first define a sine and cosine "lookup table" by

```
from numpy import pi
N = 8 # Example
theta = 2*pi/N # Example
sines = np.sin([i * theta for i in range(N)])
cosines = np.cos([i * theta for i in range(N)])
```

which can then use for convolution. Defining the values of y by `signal`, we can get the I, Q coordinates by

```
Is = (2/N) * np.convolve(signal, sines[::-1], mode='valid')
Qs = (2/N) * np.convolve(signal, cosines[::-1], mode='valid')
```

The use of `[::-1]` is by definition of the convolution operator (and likewise, the slightly ugly definition of g).

This is many orders of magnitude faster than using the `for` loop within Python.

Example in GNU Octave We first define a sine and cosine "lookup table" by

```
sines = sin([0:N-1] * theta)
cosines = cos([0:N-1] * theta)
```

which can then be used for convolution. Defining the values of y by `signal`, we can get the I, Q coordinates by

```
Is = (2/N)*conv(signal, fliplr(sines), "same")
Qs = (2/N)*conv(signal, fliplr(cosines), "same")
```

Example in Mathematica We first define a sine "lookup table" by

```
Nv = 8 (*Example*)
theta = 2*Pi/Nv (*Example*)
sines = Sin[(Range[Nv]-1)*theta]
cosines = Cos[(Range[Nv]-1)*theta]
```

which can then be used for convolution. Defining the values of y by `signal`, we can get the I, Q coordinates by

```
Is = ListConvolve[Reverse[sines], signal]
Qs = ListConvolve[Reverse[cosines], signal]
```

For reference, I also note that another strong example of convolution used is in obtaining $\Delta\phi_i$ in Equation (A.3).

Appendix B

2π Jumps Error Correction Algorithm

This appendix is written to supplement a tangential discussion on work that was done in the process of the project, as aforementioned in Section 4.3. In this section, we let ϕ_i be the individual timesteps t_i of the demodulated optical phase difference $\phi_d(t_i)$, rather than the argument of the I, Q coordinate, as given by $\tan^{-1}(Q/I)$—the measured phase.

Initial Attempt to Error Correction Algorithm When taking a closer look at the ϕ_d data generated (such as in Figure 4.4a), a recurring pattern one quickly observes is that the phase is likely to have a 2π jump when

$$|\phi_{i+1} - \phi_i| \gg 0,$$

where $\pi/2$ plays the role of expected phase change here, such in the case of $N = 4$, as presented in the context of Section 4.3. In principle, this algorithm can also be extended to the case of Chapter 5 if necessary, but will not be discussed here. To formalize the notion of $\gg 0$ as presented in the above equation, one can take a look at the distribution of $\phi_{i+1} - \left(\phi_i + \frac{\pi}{2}\right)$; This allows us to specify a choice of tolerance δ such that a phase advancement of ϕ_i to ϕ_{i+1} with

$$|\phi_{i+1} - \phi_i| > \delta$$

is considered anomalous/'large'. Successive anomalous phase advancement of the same sign are then added up until the phase advancements returns to being non-anomalous. If the total sum is approximately 2π, the algorithm can then shift the all subsequent ϕ_d by appropriate multiples of 2π. We denote the number of consecutively anomalous phase increments (or decrements) by n.

Issues with intial attempt This algorithm has several hyperparameters of arbitrary choice to nail down.

First, there are two parameters $\epsilon_\pm$ associated to the phrase "approximately 2π". Next there are 2 parameters to bound the expected values of n from below and above, which are also implicitly variable with δ. Very often, a strict choice (i.e. large) of δ would have meant that a 2π jump might have occurred with just $n = 2$, which is a very low treshold for n, and also required the parameters $\epsilon_\pm$ to have been much larger.

Alternatively, one could relax the tolerance δ, but the value of n could have then even raised to 5, and a stricter to choice of $\epsilon_\pm$ would have been harder to have narrowed down on.

While it is entirely possible to perform some kind of machine learning (probably, a grid search from gut instinct) to narrow down on the appropriate choice of parameters, such effort would prove to be wasteful with just some thought, as the noise exhibited in ϕ_d has been shown to vary with the environment, and even the length of fibre, where the choice of parameters would likely need to change.

As such, this algorithm shall be left in this appendix in words, and no code is replicated here. We now present a slightly wiser algorithm.

Second attempt to the Error Correction Algorithm In the case of $N = 4$, as prior mentioned, one does not expect $n \geq 8$ for reasonable choices of δ, even if small. As such, we define a 'difference window' $d = 8$, and a cache of length $8d$. The difference window is done across the cache. In the difference window, a 2π jump has occurred if

1. Within any given window, there is indeed a jump of approximately 2π, i.e.:

$$|\phi_{i+d} - \phi_i| \approx 2\pi,$$

2. Within the cache but outside the found window, the phase is relatively constant.

The second condition is necessary, as it is physically possible for consecutive 2π shift over all windows within the cache. This removes away the arbitrary choice of δ, but the idea of when a change is large enough to start accounting for consecutive sign difference is still useful.

The figure in the following flowchart gives a pictorial representation of what things look like during a jump.

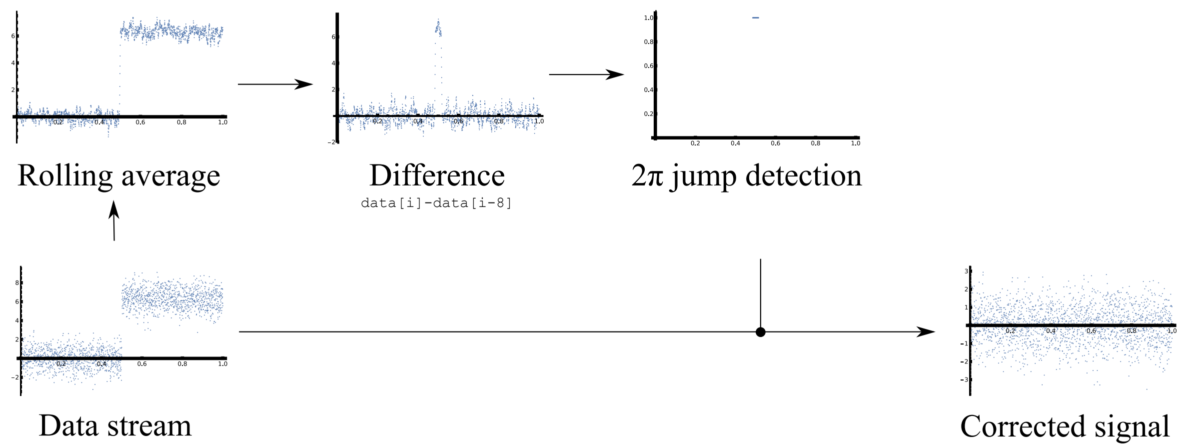

Figure B.1: Flowchart of idea to tackling 2π jumps.

Due to the constraint to keeping as minimal computations as possible, alot of the code is done in a convoluted manner. The code as in python, is as follows.

```python
import numpy as np

from math import copysign
sign = lambda x: 0 if x == 0 else int(copysign(1,x))

class fix2pi():
    def __init__(self):
        self.stream = []
        self.shift = 0
        self.shift_counter = 0
        self.prevjump = 0
        self.buflen = 0
        self.cutoff = 64
        self.rollen = 8
        self.rolavg = []
        self.counter = 0
        self.tol = 1 # 2 * rms(noise) + a bit more

    def process(self,data):
        # main loop that takes in
        data += self.shift*2*pi
        self.stream.append(data)
        self.counter +=1

        # when buffer is not filled, populate and terminate fn call
        # move data from stream into rolavg
        if self.buflen != self.cutoff:
            self.buflen +=1
            if self.buflen == self.rollen:
                self.rolavg.append(sum(self.stream)/self.rollen)
            elif self.buflen >= self.rollen:
                self.rolavg.append( \
                    (self.stream[-1]-self.stream[-1-self.rollen])
                        /self.rollen+self.rolavg[-1] )
            return None
        # addition of 2 numbers to get rolling average
        self.rolavg.append( \
            (self.stream[-1]-self.stream[-1-self.rollen])
                /self.rollen+self.rolavg[-1] )

        # check if jump is centered around 2 pi
        jump = self.rolavg[-1] - self.rolavg.pop(0)
        jump_sub = abs(jump) - 2*np.pi
        if abs(jump_sub) < self.tol: # check the signs are the same
            if sign(jump) == self.prevjump:
                self.shift_counter += 1
            else:
                self.shift_counter = max(0, self.shift_counter-1)
        else:
            self.shift_counter = max(0, self.shift_counter-1)
        self.prevjump = sign(jump)
```

```
        # print(f"{jump_sub = }, {self.prevjump = }")
        # with jump criteria satisfied, perform correction
        if self.shift_counter >= self.cutoff - self.rollen -23:
            print(f"jump detected at {self.counter:>10}")
            self.shift_counter = 0
            # implement shift
            self.shift -= self.prevjump
            # change rolling average
            jump_arg = np.argmax( \
                [abs(self.stream[i]-self.stream[i-1]) \
                    for i in range(1, self.buflen)] ) + 1
            for i in range(jump_arg, self.buflen+1):
                self.stream[i] -= self.prevjump * 2 * pi
            for i in range(max(0,jump_arg-self.rollen), \
                min(jump_arg,self.cutoff-self.rollen+1)):
                self.rolavg[i] -= self.prevjump
                    *(i-jump_arg)*2*pi/self.rollen
            for i in range(jump_arg,self.cutoff-self.rollen+1):
                self.rolavg[i] -= self.prevjump*2*pi

        return self.stream.pop(0)
```

The code is mostly self-explanatory.

The optimisations done are to utilise a rolling average to reduce the extent of noise in the phases (denoted as `stream`). The rolling average is done this way to avoid the need to recompute over all of `rollen` ("roll length") each and every time a new phase is piped in. After performing `jump = self.rolavg[-1] - self.rolavg.pop(0)`, there exists a small spike into 2π with some widdth if there has been a 2π jump. If the correct number of consecutive sign changes have occurred concurrently (i.e. the width is appropriate), as given by `shift_counter`, the 2π fix is invoked. The point within the array is manually pointed out for the rising and falling edges.

However, there are still some parameters that are fairly arbitrary, such as the 23, and the noise tolerance ϵ. As reiterated from the initial attempt, whilst it may be possible to converge on the appropriate hyperparameters, it is likely to vary between various noise situations, and therefore unlikely to be practical.

Bibliography

[1]Toshinori Sato, Junzo Kasahara, Tuncay Taymaz, Masakazu Ito, Aya Kamimura, Tadaaki Hayakawa, and Onur Tan, "A study of microearthquake seismicity and focal mechanisms within the sea of marmara (nw turkey) using ocean bottom seismometers (obss)", Tectonophysics **391**, 303–314 (2004).

[2]Christine Deplus, Michel Diament, Hélène Hébert, Guillaume Bertrand, Stéphane Dominguez, Jacques Dubois, Jacques Malod, Philippe Patriat, Bernard Pontoise, and Jean-Jacques Sibilla, "Direct evidence of active deformation in the eastern indian oceanic plate", Geology **26**, 131–134 (1998).

[3]Barbara Romanowicz, Paul McGill, Doug Neuhauser, and David Dolenc, "Acquiring real time data from the broadband ocean bottom seismic observatory at monterey bay (mobb)", Seismological Research Letters **80**, 197–202 (2009).

[4]Giuseppe Marra, Cecilia Clivati, Richard Luckett, Anna Tampellini, Jochen Kronjäger, Louise Wright, Alberto Mura, Filippo Levi, Stephen Robinson, André Xuereb, Brian Baptie, and Davide Calonico, "Ultrastable laser interferometry for earthquake detection with terrestrial and submarine cables", Science **361**, 486–490 (2018).

[5]TeleGeography Submarine Telecoms Forum, *Submarine telecoms industry report*, 5 (CreateSpace Independent Publishing Platform, 2016).

[6]Bruce M. Howe, Brian K. Arbic, Jérome Aucan, Christopher R. Barnes, Nigel Bayliff, Nathan Becker, Rhett Butler, Laurie Doyle, Shane Elipot, Gregory C. Johnson, Felix Landerer, Stephen Lentz, Douglas S. Luther, Malte Müller, John Mariano, Kate Panayotou, Charlotte Rowe, Hiroshi Ota, Y. Tony Song, Maik Thomas, Preston N. Thomas, Philip Thompson, Frederik Tilmann, Tobias Weber, and Stuart Weinstein, "Smart cables for observing the global ocean: science and implementation", **6**, `10.3389/fmars.2019.00424` (2019).

[7]CR Barnes, "Quantum leap in platforms of opportunity: telecommunication cables", Challenges and innovations in ocean in-situ sensors: Measuring Inner Ocean Processes and Health in the Digital Age, eds E. Delory and J. Pearlman (Amsterdam: Elsevier Science), 33–44 (2018).

[8]Nathaniel J Lindsey, T Craig Dawe, and Jonathan B Ajo-Franklin, "Illuminating seafloor faults and ocean dynamics with dark fiber distributed acoustic sensing", Science **366**, 1103–1107 (2019).

[9]Maria R Fernandez-Ruiz, Marcelo A Soto, Ethan F Williams, Sonia Martin-Lopez, Zhongwen Zhan, Miguel Gonzalez-Herraez, and Hugo F Martins, "Distributed acoustic sensing for seismic activity monitoring", APL Photonics **5**, 030901 (2020).

[10]Zhongwen Zhan, "Distributed acoustic sensing turns fiber-optic cables into sensitive seismic antennas", Seismological Research Letters **91**, 1–15 (2020).

[11]Yuanyuan Shan, Wenbin Ji, Xinyong Dong, Lu Cao, Mohammadmasoud Zabihi, Qing Wang, Yixin Zhang, and Xuping Zhang, "An enhanced distributed acoustic sensor based on uwfbg and self-heterodyne detection", Journal of Lightwave Technology **37**, 2700–2705 (2019).

[12]Mulugeta C Fenta, David K Potter, and Janos Szanyi, "Fibre optic methods of prospecting: a comprehensive and modern branch of geophysics", Surveys in Geophysics **42**, 551–584 (2021).

[13]Nathaniel J Lindsey, Eileen R Martin, Douglas S Dreger, Barry Freifeld, Stephen Cole, Stephanie R James, Biondo L Biondi, and Jonathan B Ajo-Franklin, "Fiber-optic network observations of earthquake wavefields", Geophysical Research Letters **44**, 11–792 (2017).

[14]Philippe Jousset, Thomas Reinsch, Trond Ryberg, Hanna Blanck, Andy Clarke, Rufat Aghayev, Gylfi P Hersir, Jan Henninges, Michael Weber, and Charlotte M Krawczyk, "Dynamic strain determination using fibre-optic cables allows imaging of seismological and structural features", Nature communications **9**, 1–11 (2018).

[15]Lutang Wang and Nian Fang, "Applications of fiber-optic interferometry technology in sensor fields", Optical Interferometry (2017).

[16]Scott Rashleigh, "Origins and control of polarization effects in single-mode fibers", Journal of Lightwave Technology **1**, 312–331 (1983).

[17]Eric Udd and William B Spillman Jr, *Fiber optic sensors: an introduction for engineers and scientists* (John Wiley & Sons, 2011).

[18]Jennifer Watchi, Sam Cooper, Binlei Ding, Conor M. Mow-Lowry, and Christophe Collette, "Contributed review: a review of compact interferometers", Review of Scientific Instruments **89**, 121501 (2018).

[19]T Schilcher, "RF applications in digital signal processing", in Cas - cern accelerator school: course on digital signal processing (2008), pages 249–283.

[20]Steven B Damelin and Willard Miller, *The mathematics of signal processing*, Cambridge texts in applied mathematics, 48 (Cambridge University Press, 2011).

[21]Walter Rudin, *Real and complex analysis: 3rd. ed.* (McGraw-Hill, 1987).

[22]Kurt Jacobs, *Stochastic processes for physicists: understanding noisy systems* (Cambridge University Press, 2010).

[23]Simon Haykin and Bernard Widrow, *Least-mean-square adaptive filters*, Vol. 31 (John Wiley & Sons, 2003).